NASA Technical Memorandum 4338

# Design, Test, and Evaluation of Three Active Flutter Suppression Controllers

William M. Adams, Jr.
*Langley Research Center*
*Hampton, Virginia*

David M. Christhilf
*Lockheed Engineering & Sciences Company*
*Hampton, Virginia*

Martin R. Waszak and Vivek Mukhopadhyay
*Langley Research Center*
*Hampton, Virginia*

S. Srinathkumar
*National Aeronautical Laboratory*
*Bangalore, India*

National Aeronautics and
Space Administration
Office of Management
Scientific and Technical
Information Program
1992

(NASA-TM-4338) DESIGN, TEST, AND
EVALUATION OF THREE ACTIVE FLUTTER
SUPPRESSION CONTROLLERS (NASA)
41 p

N93-10070

Unclas

H1/05 0122412

# Abstract

*Three control law design techniques for flutter suppression are presented. Each technique uses multiple control surfaces and/or sensors. The first method uses traditional tools (such as pole/zero loci and Nyquist diagrams) for producing a controller that has minimal complexity and which is sufficiently robust to handle plant uncertainty. The second procedure uses linear combinations of several accelerometer signals and dynamic compensation to synthesize the modal rate of the critical mode for feedback to the distributed control surfaces. The third technique starts with a minimum-energy linear quadratic Gaussian controller, iteratively modifies intensity matrices corresponding to input and output noise, and applies controller order reduction to achieve a low-order, robust controller. The resulting designs have been implemented digitally and tested subsonically on the active flexible wing wind-tunnel model in the Langley Transonic Dynamics Tunnel. Only the traditional pole/zero loci design was sufficiently robust to errors in the nominal plant to successfully suppress flutter during the test. The traditional pole/zero loci design provided simultaneous suppression of symmetric and antisymmetric flutter with a 24-percent increase in attainable dynamic pressure. Posttest analyses are shown which illustrate the problems encountered with the other laws.*

## Introduction

Aircraft designs that emphasize the reduction of structural weight to maximize efficiency and agility increase the likelihood that active flutter suppression will be needed to remove structural dynamic instabilities. In such cases, active flutter suppression can potentially enable achievement of enhanced performance with lower weight. Developing methods to suppress flutter and reduce structural loads has been an objective of the active flexible wing (AFW) program.

Active controls, with flutter suppression as a specific example, are recognized to provide maximum performance benefits when their impact is considered early in the aircraft design process. Providing a complete summary of the current status of active controls research is beyond the scope of this paper; however, selected references are cited which are representative of published work in the areas of flutter suppression and gust load alleviation (refs. 1 to 29). A reference describing the historical development of flutter research is also cited (ref. 30).

This paper describes the design, test, and evaluation of three flutter suppression control laws. The designs were part of a joint effort by Langley Research Center and Rockwell International Corporation to validate analysis and synthesis methodologies through the development of digital multi-input/multi-output control laws for an aeroelastic wind-tunnel model (refs. 31 and 32). The test vehicle used in this effort is the Rockwell AFW wind-tunnel model (ref. 33), which was modified from its initial configuration through the use of wing tip stores containing destabilizing mass ballast. The test results described in this paper refer to a model entry in the Langley Transonic Dynamics Tunnel (TDT) in November 1989. A subsequent test was performed in March 1991 during which four flutter suppression control laws were successfully tested during steady flight and while performing aggressive rolling maneuvers (refs. 34 to 37).

The wind-tunnel model, test operating constraints, tunnel turbulence model, uncontrolled flutter characteristics, and controller design constraints are described to provide an understanding of the controller design problem. The design objective is to control flutter to the tunnel limit without saturating control power capabilities.

Three controllers have been designed, all of which use multiple control surfaces and/or sensors. The first controller uses traditional tools (pole/zero loci and Nyquist diagrams, ref. 38); the second uses accelerometer output blending and control command distribution to obtain an estimate of the flutter mode rate for feedback (refs. 11, 19, and 25). The third controller uses linear quadratic Gaussian (LQG)/loop transfer recovery (ref. 39) plus order reduction (ref. 40). The design approach for each is described, and predicted controller performance is shown. Test results are also discussed which show that only the traditional pole/zero loci design was sufficiently robust to modeling errors to suppress flutter during the test. Posttest analyses are presented which explain the problems that were encountered with the other laws.

## Symbols

| | |
|---|---|
| $a$ | parameter in washout filter element in control laws |
| $a_1, a_2$ | filter parameters in modal rate feedback control law (see fig. 9) |
| $(a_{d_j}, \zeta_{d_j}, \omega_{d_j})$ | parameters in rational transfer function representation of $j$th actuator |
| $b_s$ | wing semispan of wind-tunnel model |
| $\mathbf{B}_{\mathrm{LN}}$ | matrix of sensor blending coefficients (see eq. (4)) |
| $\tilde{\mathbf{B}}$ | output of sensor blending operation (see fig. 9) |
| $\mathbf{H}_d'$ | $= \mathbf{H}_d\mathbf{F}_d$ (see eq. (3)) |
| $\mathbf{E}_d'$ | $= \mathbf{H}_d\mathbf{G}_d + \mathbf{E}_d$ (see eq. (3)) |
| $\mathbf{D}_{\mathrm{IS}}$ | matrix defining distribution of pseudo-control command to physical control surfaces (see eq. (4)) |
| $d$ | scalar multiplier defining proportion of control command $\delta_{\mathrm{TEO}_c}$ that is to go to $\delta_{\mathrm{TEI}_c}$ (see eq. (1)) |
| $\mathbf{E}, \mathbf{E}_d$ | control law feedthrough term (see eqs. (3) and (9)) |
| $\mathbf{F}, \mathbf{F}_d$ | control law system matrix (see eqs. (2) and (9)) |
| $f$ | frequency, Hz |
| $\mathbf{G}, \mathbf{G}_d$ | control law input matrix (see eqs. (2) and (9)) |
| $g$ | acceleration due to gravity |
| $\mathbf{H}, \mathbf{H}_d$ | control law matrix relating outputs to states (see eqs. (3) and (9)) |
| $\mathbf{I}$ | identity matrix |
| $i$ | $= \sqrt{-1}$ |
| $J$ | augmented function to be minimized in design of modal rate feedback control law (see eq. (7)) |
| $\mathbf{K}_1, \mathbf{K}_2, \mathbf{K}_3$ | control law transfer matrices (see eqs. (1), (4), and (9)) |
| $k$ | gain in desired transfer function at single strand point (see eq. (6)) |
| $k_1, k_2$ | scalar feedback gains in control laws (see eqs. (1) and (4)) |
| $k_-$ | smallest magnitude intersection of loop transfer function with negative real axis to left of the $-1$ point (see fig. 11); the larger $k_-$ is the more tolerant the system is to gain decrease |
| $k_+$ | largest magnitude intersection of loop transfer function with negative real axis to right of the $-1$ point (see fig. 11); the smaller $k_+$ is the more tolerant the system is to gain increase |
| $\phi_-$ | smallest magnitude angle between negative real axis and intersection of loop transfer function with unit circle in either of first two quadrants (see fig. 11); the larger $\phi_-$ is the more tolerant the system is to errors in lead |
| $\phi_+$ | smallest magnitude angle between negative real axis and intersection of loop transfer function with unit circle in either quadrant 3 or quadrant 4 (see fig. 11); the larger $\phi_+$ is the more tolerant the system is to errors in lag |
| $\mathbf{M}_\delta$ | controller/generalized coordinate mass coupling matrix |
| $m_i$ | $i$th diagonal element of generalized mass matrix |
| $m_\delta$ | number of controls used in law (see eq. (7)) |
| $N_1, N_2, N_3$ | second-order notch filters that make up band-rejection filter |
| $n_\omega$ | number of frequencies (see eq. (7)) |
| $\mathbf{P}_1, \mathbf{P}_2, \mathbf{P}_3$ | design plant transfer matrices (see figs. 6, 9, and 13) |
| $q$ | dynamic pressure |
| $\mathbf{Q}_\xi, \mathbf{Q}_\delta, \mathbf{Q}_g$ | generalized aerodynamic force matrices |
| $R$ | desired transfer function at single-strand point (see eq. (6)) |

| | |
|---|---|
| $s$ | Laplace variable |
| $T$ | time between samples |
| $\mathbf{T}_2$ | matrix defining dynamic portion of modal rate feedback control law (see fig. 9) |
| $T_{SS}$ | analytically predicted loop transfer function at single-strand point in modal rate feedback control law (see eq. (5)) |
| $T_{d_j}$ | rational transfer function approximation of $j$th actuator |
| $U$ | pseudo-control command (see fig. 9) |
| $u_k$ | output of digital control law at $k$th time step (see eq. (2)) |
| $V$ | fluid velocity |
| $W_{\delta_m}$ | weight associated with violation of $m$th actuator rate constraint (see eq. (7)) |
| $W_{\omega_n}$ | weight associated with cost $J$ (see eq. (7)) |
| $W_g$ | gust velocity |
| $x, x_0$ | general and reference streamwise coordinate |
| $\mathbf{x}_k$ | discrete controller state at $k$th time step |
| $\mathbf{x}_u$ | continuous controller state for LQG law (see eq. (9)) |
| $y$ | spanwise coordinate |
| $\mathbf{y}_k$ | input to digital control law at $k$th time step (see eq. (2)) |
| $\ddot{\mathbf{z}}$ | vector of accelerometer outputs |
| $\hat{\dot{z}}_f, \dot{z}_f$ | achieved and desired flutter modal rate (see figs. 9 and 10) |
| $\alpha_g$ | incremental angle of attack due to turbulence |
| $\boldsymbol{\delta}$ | vector of control surface deflections |
| $\delta_{jk}$ | Kronecker delta with value 0 for distinct indices and 1 if $j = k$ |
| $\delta(\omega - \omega_0)$ | Dirac delta with properties: $\delta(\omega - \omega_0) = 0$ if $\omega \neq \omega_0$ and $\int_{-\infty}^{\infty} f(\omega)\ \delta(\omega - \omega_0)\ d\omega = f(\omega_0)$ |
| $(\dot{\delta}_{m_c})_{\text{rms}}$ | rms commanded rate for $m$th actuator |
| $\zeta$ | damping ratio |
| $\eta$ | white-noise input into Dryden filter |
| $\sigma$ | singular value |
| $\sigma_{g_S}, \sigma_{g_A}$ | rms symmetric and antisymmetric turbulence velocities, respectively |
| $\tau$ | time delay |
| $\Phi_{w_g}$ | Dryden turbulence power spectral density |
| $\omega$ | frequency, rad/sec |
| $\omega_g$ | break frequency in Dryden turbulence representation |

Subscripts:

| | |
|---|---|
| $A$ | antisymmetric |
| $c$ | commanded |
| $D$ | denominator |
| $d$ | digital representation of controller |
| $f$ | flutter |
| $n$ | natural frequency |
| $N$ | numerator |
| $S$ | symmetric |

Notation:

Bold symbols refer to matrix or vector quantitites.

| | |
|---|---|
| $(\underline{\ })$ | bar under symbol indicates that it is a minimum of ( ) |
| $(\overline{\ })$ | bar over symbol indicates that it is a maximum of ( ) |
| $(\dot{\ })$ | dot over symbol indicates time derivative of ( ) |

Abbreviations:

| | |
|---|---|
| A | analog |
| AAF | antialiasing filter |
| AFS | active flutter suppression |
| AFW | active flexible wing |
| BRF | band-rejection filter (see eq. (8)) |
| conj | conjugate |
| CPE | controller performance evaluation |
| D | digital |

ORIGINAL PAGE
BLACK AND WHITE PHOTOGRAPH

| | |
|---|---|
| dof | degree of freedom |
| DNOT | notch filter to be implemented digitally (see "Modal Rate Feedback Control Law Definition" section of appendix) |
| INT1, INT2 | stable integrators (see "Modal Rate Feedback Control Law Definition" section of appendix) |
| LEI | leading edge inboard |
| LEO | leading edge outboard |
| LQG | linear quadratic Gaussian |
| max | maximum |
| MIMO | multi-input/multi-output |
| min | minimum |
| MISO | multi-input/single output |
| PSD | power spectral density |
| rms | root mean square |
| SISO | single input/single output |
| TDT | Transonic Dynamics Tunnel |
| TEI | trailing edge inboard |
| TEO | trailing edge outboard |
| TIP | wing tip |
| WOF | washout filter (see "Modal Rate Feedback Control Law Definition" section of appendix) |

## AFW Wind-Tunnel Model and Test Conditions

### Wind-Tunnel Model

The AFW wind-tunnel model is a full-span, sting-mounted, wind-tunnel model that can roll about the sting axis (fig. 1). For the flutter suppression testing described herein (the TDT entry in November 1989), the AFW wind-tunnel model was prevented from rolling by applying a locking pin. The model has a six-degree-of-freedom force and moment balance on the load path to the sting and an actuator that can be used to adjust the model angle of attack. Four pairs of control surfaces exist with hinge lines near the one-quarter- or three-quarter-chord locations. The actuators for the control surfaces and for the angle-of-attack adjustment are powered by an onboard hydraulic system. The model fuselage is more rigid than the wings. However, the sting undergoes small vertical and lateral translations as well as angular twisting about the sting axis.

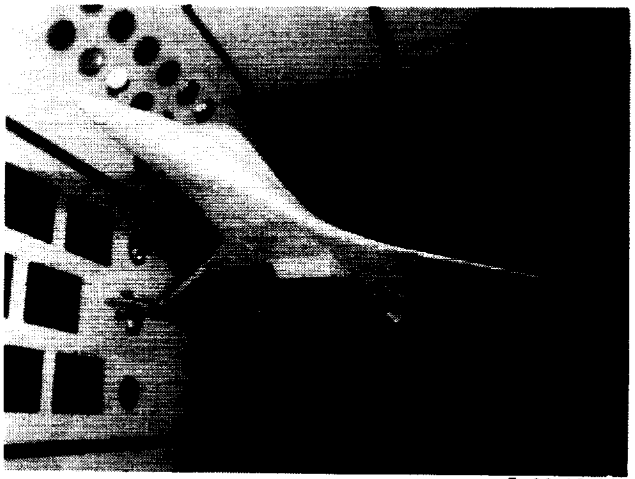

L-89-12,445

Figure 1. Active flexible wing (AFW) model in wind-tunnel test section.

Each of the three control law designs used a subset of four pairs of accelerometers and four pairs of control surfaces (fig. 2). Strain gauges on the wing were also available, but they were not used for flutter suppression during the 1989 tests. A digital computer implemented the controller that processed the signals from the accelerometers to generate commands for the control surface actuators; this process actively suppressed flutter. Signal transmission between the digital controller and the analog sensors and actuators required low-pass analog filters (to reduce aliasing) as well as analog-to-digital and digital-to-analog conversions.

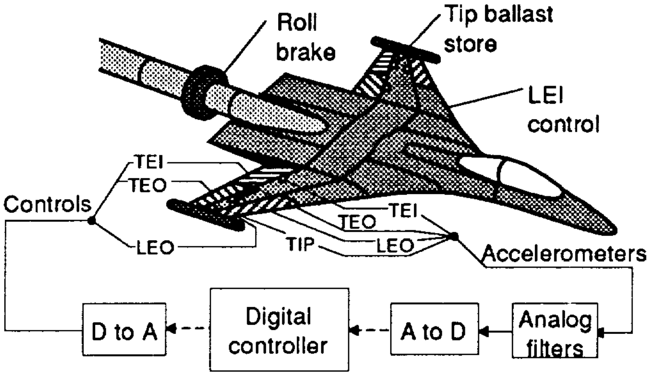

Figure 2. Sketch of AFW wind-tunnel model.

The original configuration of the AFW wind-tunnel model was previously tested using multiple control surfaces (ref. 41) to study rapid rolling maneuvers for a model with a soft, flexible wing. This configuration did not flutter within the operating range of the TDT. For the study described here, tip stores containing mass ballast were added to the AFW. The ballast lowered the frequency of the first torsion mode (bringing it closer to the frequency of the first bending mode) and, thereby, reduced the dynamic pressure at which flutter occurs to within the operational range of the wind tunnel.

The tip ballast stores, which are normally coupled in torsion with the wing via a hydraulic brake, can be decoupled by releasing the brake, thereby leaving the stores restrained in torsion by only a soft spring. Upon brake release, the decoupled configuration has flutter-free characteristics to a much higher dynamic pressure than those shown in figure 3 for the coupled case. Thus, the tip ballast stores utilize the decoupler pylon concept (ref. 42) to also provide a flutter-stopper capability. A more complete discussion of the tip ballast stores can be found in reference 43.

### Wind-Tunnel Conditions

The Langley TDT, which is specially configured for testing aeroelastic models (ref. 44), is a sealable wind tunnel in which Mach number and dynamic pressure can be varied independently by changing motor speed while simultaneously changing stagnation pressure in the tunnel through the use of pumps. For the 1989 test, air was the test medium, and the tunnel was operated in an unsealed condition at atmospheric pressure. The maximum dynamic pressure achievable in this mode was variable because it was dependent upon atmospheric conditions. At standard atmospheric pressure, a maximum dynamic pressure of approximately 325 psf could be generated at a Mach number of 0.5 (fig. 3). Higher Mach numbers required air to be pumped from the tunnel to reduce the stagnation pressure.

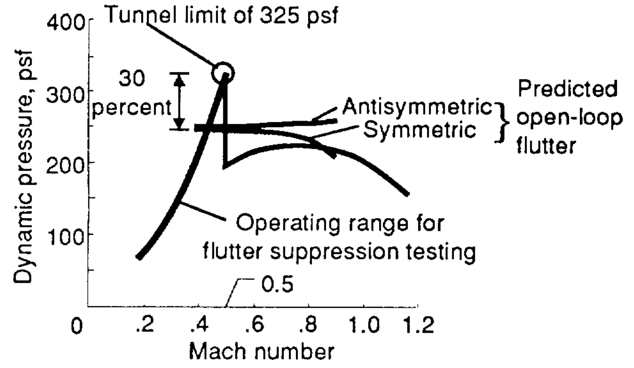

Figure 3. Wind-tunnel test conditions with air as test medium and predicted flutter characteristics for coupled configuration.

A test plan was developed which maximized the demonstrable increase in closed-loop flutter dynamic pressure and allowed rapid progression between test points. Each closed-loop test run was made at atmospheric pressure and was planned to reach a Mach number of 0.5 at the maximum achievable dynamic pressure (fig. 3). On the test path, both Mach number and dynamic pressure were simultaneously varied by increasing the fan motor speed. The Mach number variation was acceptable because Mach number effects in the low subsonic region were small. A rapid progression between test points was made possible by operating in this mode. Running at a fixed Mach number, which would involve pumping air out or bleeding air into a sealed tunnel, would have been less efficient for obtaining closed-loop data.

Wind-tunnel turbulence had a significant impact on the AFW wind-tunnel model response. Consequently, critical loads were monitored during the test, and test runs were terminated when a load exceeded a preset maximum amplitude. Prior to the test and based upon earlier tunnel entries, the turbulence was estimated to have a root-mean-square (rms) velocity of 1 ft/sec, a maximum intensity at 10 Hz, and an apportionment that was 85 percent symmetric and 15 percent antisymmetric.

## Mathematical Modeling

Linear aeroelastic descriptions for the symmetric and antisymmetric boundary conditions were generated using the Interaction of Structures, Aerodynamics, and Controls (ISAC) system of programs (ref. 45). The doublet lattice aerodynamic theory was used (ref. 46). In addition, these models were combined with empirical data to form a whole-aircraft model for a batch simulation (ref. 47) which considered quantization, computational delays, actuator position and rate limits, and asymmetries caused by differences between individual actuators.

### Actuators

Frequency responses for the eight individual actuators were measured with no air flow and with the wing elastic motion restrained. In the frequency range of interest, third-order transfer functions, with parameters optimized in a least-squares sense, produced good fits with the measured frequency response data. In general, right and left members of an actuator pair required different parameters to achieve a good fit, and, therefore, they were modeled in this manner. All the actuator transfer functions had the following form:

$$\frac{\delta_j}{\delta_{c_j}} = \frac{k_{d_j} a_{d_j} \omega_{d_j}^2}{\left(s + a_{d_j}\right)\left(s^2 + 2\zeta_{d_j}\omega_{d_j} s + \omega_{d_j}^2\right)} = T_{d_j}(s)$$

where $k_{d_j}$ is the steady-state gain, $a_{d_j}$ is the first-order pole location, $\zeta_{d_j}$ is the damping ratio of the complex pair, and $\omega_{d_j}$ is the natural frequency of the complex pair. The physical origin of these parameters is explained in reference 47. For linear analyses, averages of each parameter from members of a pair were employed to represent each member to retain decoupling between symmetric and antisymmetric degrees of freedom. However, for the batch simulation, the distinct actuator identities were retained and were sources of coupling between the two symmetries.

### Turbulence

A basic assumption made in computing symmetric aerodynamic forces caused by turbulence was that randomly generated turbulence traveled, unchanged, downstream past the model at the fluid velocity $V$. Thus, what was encountered at a reference streamwise location $(x_0, y)$ at time $t$ would be encountered at a point $(x, y)$ at a time $t + (x - x_0)/V$, where $V$ was the fluid velocity. Another assumption was that the symmetric turbulence downwash field seen at streamwise coordinate $x_0$ resulted in angle-of-attack perturbation elements of the form

$$\alpha_{g_S}\left(x_0, y, \omega_0, t\right) = \exp\left(i\omega_0 t\right)$$

which had the Fourier transform

$$\alpha_{g_S}\left(x_0, y, \omega\right) = 1\delta\left(\omega - \omega_0\right)$$

The same symbols (e.g., $\alpha_{g_S}$) are used in this paper to represent a function and its transform. The expression for the Fourier transform at an arbitrary location, relative to that at the reference streamwise coordinate, was

$$\alpha_{g_S}\left(x, y, \omega\right) = \exp\left(-i\omega_0 \frac{x - x_0}{V}\right) \delta\left(\omega - \omega_0\right)$$

The contribution, which was due to an oscillatory component of frequency $\omega_0$, to the antisymmetric turbulence was approximately proportional to the spanwise location, relative to the model centerline, with no streamwise variation. Thus, the Fourier transform for this case was

$$\alpha_{g_A}\left(x, y, \omega\right) = \frac{y}{b_s} \delta\left(\omega - \omega_0\right)$$

The parameter $b_s$ was the wing semispan. The coefficients of the Dirac delta functions in these downwash representations were used to compute generalized aerodynamic forces caused by turbulence.

The final assumptions had to do with the spectral content of the turbulence. A Dryden atmospheric turbulence model was used (ref. 48). The turbulence power spectral density was

$$\Phi_{w_g}\left(\omega\right) = \frac{\sigma^2_{w_g}}{\pi\omega_g} \frac{1 + 3\left(\frac{\omega}{\omega_g}\right)^2}{\left[1 + \left(\frac{\omega}{\omega_g}\right)^2\right]^2} \qquad \left(0 \leq \omega \leq \infty\right)$$

The following transfer function, used in the development of the state equations discussed subsequently, will produce an output with the power spectral density just shown, when receiving white-noise input $\eta$ with the power spectral density $1/\pi$:

$$\frac{w_g}{\eta}\left(s\right) = \sigma_{w_g}\sqrt{3\omega_g} \frac{s + \frac{1}{\sqrt{3}}\omega_g}{s^2 + 2\omega_g s + \omega_g^2}$$

which can be verified by using the following equality:

$$\Phi_{w_g}\left(\omega\right) = \frac{1}{\pi} \frac{w_g}{\eta}\left(i\omega\right) \frac{w_g}{\eta}\left(-i\omega\right)$$

A break frequency $\omega_g/(2\pi)$ of 17.23 Hz was used to approximate the expected wind-tunnel turbulence. Resonance peaks at 10 Hz were observed in tunnel data from prior entries, and a range from 10 Hz to 12 Hz was the predicted flutter frequency. A break frequency of 17.23 Hz produces a peak magnitude in $w_g/\eta$ at 10 Hz.

No accurate representation of the wind-tunnel turbulence levels was available. Furthermore, the effect on the plant of any given turbulence intensity would be highly dependent on the configuration and the gust mode shapes used to characterize the turbulence. Based on prior wind-tunnel entries, the rms turbulence velocity magnitude was estimated to be approximately 1 ft/sec at the wing tips at a Mach number of 0.5 and a dynamic pressure of 300 psf. This magnitude was conservatively assumed to apply at all test conditions. Eighty-five percent of the turbulence was allocated to the symmetric component, and 15 percent was allocated to the antisymmetric component at the wing tips.

In the batch simulation, a single Gaussian-distributed random number with unit standard deviation was generated at each integration time step (0.5 msec) and scaled to provide a digital approximation of continuous white noise with a power spectral density of $1/\pi$ (ref. 47). That single number was then multiplied (by either 0.85 or 0.15) and used as an input to the separate transfer functions representing symmetric and antisymmetric turbulence. Given the gust mode shapes just discussed, this process resulted in a constructive correlation on the right wing (at least at the $x_0$ location), a destructive correlation on the left wing, and a linear variation accross the span. Using two uncorrelated random numbers would have been preferable with the rms gust velocity components of $\sigma_{g_S} = 0.985$ ft/sec and $\sigma_{g_A} = 0.174$ ft/sec to achieve an 85/15 distribution whose vector sum was 1 ft/sec. The representation employed was sufficient to evaluate the potential for saturating the actuator rate capability, because the larger of the values for the left and right control surface activity was used. In the results, the predicted actuator rate rms responses will be seen to be significantly higher than those in the test actuator rate rms responses.

### Equations of Motion

*In vacuo* vibration characteristics were calculated based upon a structural model developed by Rockwell International Corporation. The structural model development benefited from experimental data obtained for the model prior to the addition of the tip ballast stores. The vibration tests were also made on the current configuration, and the results from these tests were used to adjust the predicted modal natural frequencies and, together with aeroelastic analyses, to determine which elastic modes to retain in the model. Eight symmetric and seven antisymmetric elastic modes were retained. Structural damping was modeled as being viscous with a damping ratio of 0.015 assumed for each mode.

Equations of motion were developed both in a frequency domain form, which made direct use of the tabular unsteady aerodynamic forces, and in a finite dimensional state-space form, which employed rational function approximations to the aerodynamic forces. The frequency domain form of the equations was

$$\begin{bmatrix} m_j \left[ (i\omega)^2 + 2\zeta_j \omega_{n_j} (i\omega) + \omega_{n_j}^2 \right] \delta_{jk} - q\mathbf{Q}_\xi & \mathbf{M}_\delta (i\omega)^2 - q\mathbf{Q}_\delta \\ 0 & I \end{bmatrix} \begin{pmatrix} \boldsymbol{\xi} \\ \boldsymbol{\delta} \end{pmatrix} = \begin{bmatrix} q\mathbf{Q}_g & 0 \\ 0 & T_{\delta_j} \delta_{jk} \end{bmatrix} \begin{pmatrix} \alpha_g \\ \boldsymbol{\delta}_c \end{pmatrix}$$

with accelerometer outputs of the form

$$\ddot{z}_j = (i\omega)^2 \mathbf{\Pi} (x_j, y_j) \boldsymbol{\xi} (\omega)$$

A display of the dependence of the unsteady aerodynamic forces upon frequency and Mach number was suppressed for brevity and clarity. All the mathematical models were generated with the aerodynamic force coefficient data corresponding to a Mach number of 0.5, regardless of velocity, because Mach number effects in the low subsonic region of the test were small. This approximation became more precise as the tunnel operating limit was approached. The row vector $\mathbf{\Pi}(x_j, y_j)$ relates the $j$th output to unit displacements of the generalized coordinates $\boldsymbol{\xi}$. The Kronecker delta $\delta_{jk}$ is zero unless the indices match, in which case it is unity. This form of the equations allowed the numerical computation of a frequency response function for any output/input pair. Consequently, for a stable system, power spectral densities and rms values for any output could also be computed. The modal rate feedback design approach used design models with the frequency domain form.

Rational function approximations were made to the unsteady aerodynamic forces to obtain finite dimensional state-space models. Reference 49 presents this approach. The same single lag factor per mode was judged to sufficiently represent the unsteady aerodynamic effects, while keeping the number of states manageable. The resulting state-space models with three pairs of actuators retained were 35th order symmetrically and 32nd order antisymmetrically. State-space plant representations were employed in the traditional pole/zero loci and modified LQG design approaches. Reference 47 presents the structure of the state-space models and the additions necessary to generate the batch simulation.

## Controller Design Considerations in Active Flutter Suppression

### Flutter Character

For the 1989 test described here, the model was fixed in roll. This condition, together with the nearly rigid fuselage, caused the characteristics of the AFW wind-tunnel model symmetric and antisymmetric flutter to be similar. The predicted flutter dynamic pressures at a Mach number of 0.5 (see fig. 3) were 248 psf for the symmetrical and 252 psf for the antisymmetrical cases. Therefore, the simultaneous operation of a control law for each symmetry was required. The flutter frequency in each case was predicted to be approximately 11.5 Hz. The flutter characteristics were relatively explosive; at a dynamic pressure of 325 psf, the predicted time for the flutter mode to double in amplitude was approximately 1/10 sec.

### Control Law Implementation Considerations

Each of the three active flutter suppression (AFS) control laws was designed in the continuous domain. The assumption was made that no coupling existed between the symmetric and antisymmetric response for the AFW wind-tunnel model. Figure 4 illustrates how the symmetric and antisymmetric forms of the control laws were implemented simultaneously by the digital controller (ref. 50). For each pair of accelerometers, the symmetric signal was determined as the average of the right and left signals, and the antisymmetric signal was determined as one-half of the difference between the right and left signals. Similarly, the right and left control surface commands were determined as the sum and difference of the symmetric and antisymmetric commands for each pair of control surfaces.

The trailing-edge outboard (TEO) control surfaces (see fig. 2) were the most effective in controlling flutter, although the actuator hinge moment available for these surfaces was only one-half as large as the others because each TEO surface was driven by one actuator rather than two; the use of a single actuator was due to the limited space available in the outboard portion of the wing. The leading-edge-outboard (LEO) surfaces have unfavorable aerodynamic loading that does not restore the surfaces to a neutral position if the actuators become overloaded. The trailing-edge-inboard (TEI) surfaces have favorable aerodynamic loading, but they are not as effective as the TEO surfaces in controlling flutter. The leading-edge-inboard (LEI) control surfaces had higher inertias and less aerodynamic effect upon the flutter mechanism and were, therefore, not suitable for FSS control. Each of the wing accelerometer pairs was located near the hinge line of one of the control surface pairs, with

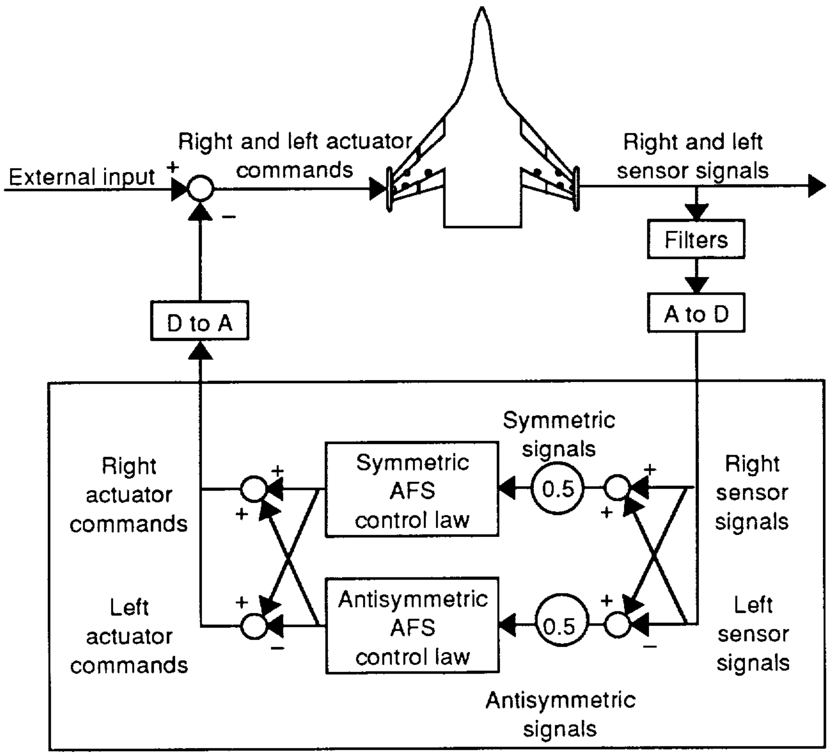

External input
+
−
Right and left actuator commands
Right and left sensor signals
Filters
A to D
D to A
Symmetric signals
Right actuator commands
+
+
Symmetric AFS control law
0.5
+
+
Right sensor signals
Left actuator commands
+
−
Antisymmetric AFS control law
0.5
+
−
Left sensor signals
Antisymmetric signals

Figure 4. Implementation of symmetric and antisymmetric AFS control laws.

the exception of the wing tip (TIP) accelerometers that were located approximately midchord near the wing tips. The TIP accelerometers responded to the flutter mode and, at the same time, were relatively unresponsive to the higher frequency modes when compared with the other accelerometers.

The digital implementation of the control laws had certain implications for the control law designer. The sample rate was 200 Hz. A low-pass analog antialiasing filter was required for each channel being digitized to attenuate signal strength above the Nyquist frequency (100 Hz in this case), so that higher frequency harmonic signals would not corrupt the lower frequency signals caused by the periodic sampling. Two viable choices of analog antialiasing filters were provided. The choices were a first-order filter with a break frequency of 25 Hz and a fourth-order Butterworth filter with a break frequency of 100 Hz. Each of these introduced approximately the same lag in the flutter frequency range (near 10 Hz). Only the first-order filter was used during the test, principally because it provided some attenuation of outputs that were due to structural modes in the 30- to 40-Hz range; these outputs were outside the desired control bandwidth but within the actuator bandwidth. A first-order filter with a break frequency of 100 Hz and a fourth-order Butterworth filter with a break frequency of 25 Hz were also available; these filters were not viable candidates because of the lack of antialiasing protection from the former and the excess phase lag from the latter.

The signal amplitude was quantized because the analog-to-digital and digital-to-analog converters had 12 bits of resolution. Using an accelerometer signal as an example and assuming that the accelerometer signals had a range of $40g$ ($\pm 20g$) led to a quantization of approximately $0.01g$. This quantization level is of little concern unless the controller has an extremely high gain such as would occur at low frequency for a pure integrator.

An effective average 0.5 time step delay was introduced by the sampling because, after a signal was sampled at the beginning of a time step, no additional information was passed until the beginning of the next time step. The control laws were implemented in the digital computer so that control commands generated based on sensor inputs received at one sampling instant were held (before being sent out) for a time $\tau_h$ such that the sum of $\tau_h$ and $\tau_c$ (the time required to compute the outputs) was 5 msec (one time step). Thus, approximately a 1.5 time step delay was present as a result of these aspects of the digital implementation as compared with a continuous implementation.

Each of the controllers was designed in the continuous domain and implemented digitally by using a Tustin transformation with no frequency prewarping (ref. 51). The method chosen for transformation of a continuous controller to a discrete form also impacts the digital time delay. The net time delays assumed in the three designs will be shown below.

## Design Objectives and Requirements

The design objective for all three flutter suppression control laws was to demonstrate closed-loop stability up to the wind-tunnel limit of 325 psf dynamic pressure. This objective would constitute a 30-percent increase in the flutter dynamic pressure relative to the lowest predicted open-loop flutter boundary in the subsonic region.

For those control laws that had a single-strand (i.e., single-channel) point in the feedback loop, a predicted gain margin of ±6 dB and a predicted phase margin of ±30° with respect to that point were required throughout the test envelope. (This phase requirement was a relaxation from an earlier, unachieved, requirement of 45°.) If the law was not truly single input/single output (SISO), then the simple gain and phase margins were a potentially nonconservative assessment of robustness, and they will be shown to be a source of poor controller performance for one of the control laws. The control law that utilized multi-input/multi-output (MIMO) analysis was judged by potentially conservative multi-variable margins, and the stated requirements were relaxed for that case to correspond to the predicted robustness achieved.

Actuator rate saturation can degrade control law performance and lead to closed-loop instability. At the wind-tunnel limit of 325 psf, the open-loop time-to-double amplitude for the symmetric flutter mode was predicted to be 1/10 sec. For this instability level, actuator rate saturation of a pair of actuators for even a brief time in response to wind-tunnel turbulence could cause an unacceptably large growth of the flutter mode. This potential for rate saturation reinforced the need to restrict actuator rate requirements. The TEO control surfaces were predicted to have a peak no-load aerodynamic rate capability of 225 deg/sec. It was assumed that no rate saturation for a three-standard-deviation turbulence velocity magnitude was adequate for assuring that rate saturation was sufficiently unlikely (ref. 52). A one-standard-deviation actuator rate of 75 deg/sec resulted. At a predicted flutter frequency of approximately 11.5 Hz, this rate constraint translated to a maximum rms control deflection of 1° (i.e., the

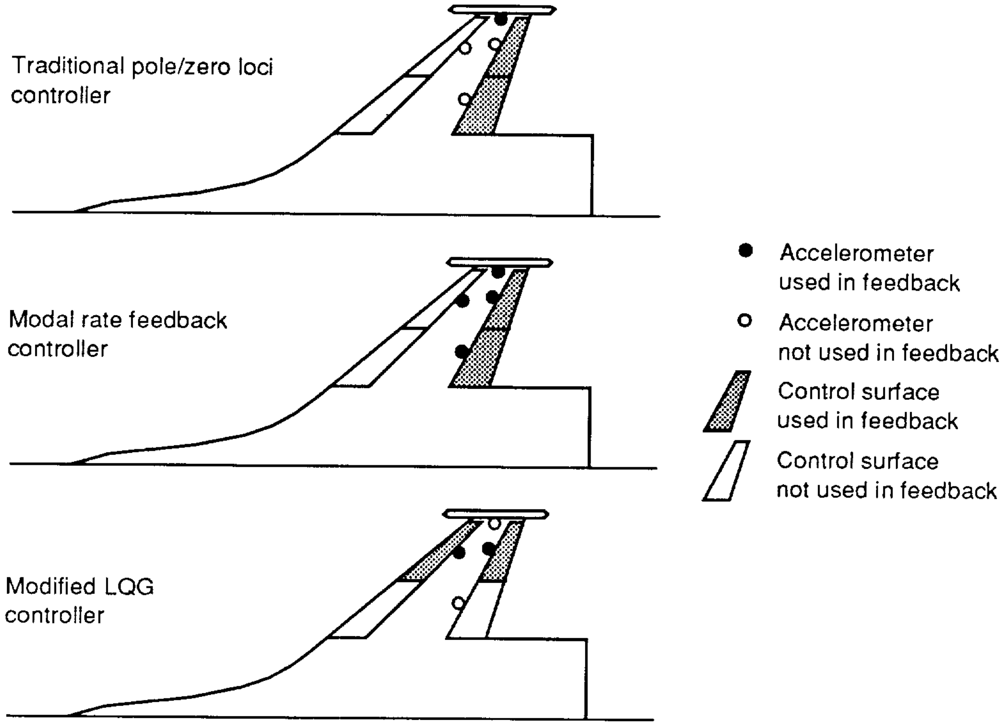
Traditional pole/zero loci controller
Modal rate feedback controller
Modified LQG controller
● Accelerometer used in feedback
○ Accelerometer not used in feedback
Control surface used in feedback
Control surface not used in feedback

Figure 5. Sensors and control surfaces used by each control law.

maximum deflection that would occur if all control power was concentrated at the flutter frequency).

Another requirement for evaluating candidate control laws prior to the wind-tunnel entry was to demonstrate closed-loop stability throughout the test envelope using a batch simulation (ref. 47). As discussed, the simulation replicated quantization effects because of finite word length in the signal converters and imposed rate and displacement limits on the control surface actuators. This simulation also allowed both symmetries to be run simultaneously in the presence of simulated turbulence excitation with a separate dynamic actuator model for each left and right control surface.

## Design and Analysis of Active Flutter Suppression Controllers

Three active control laws for flutter suppression were designed in the continuous domain, implemented digitally, and tested in the TDT. The darkened areas in figure 5 show the sensors and control surfaces employed in each law. The next three subsections present the design approach and pretest analysis of performance for each control law. The approaches are presented in the order of increasing mathematical complexity.

### Traditional Pole/Zero Loci Design (Design Number 1)

***Overview.*** This control law was designed using traditional complex plane mappings of poles and zeros. The principal philosophy behind this design effort was to avoid getting lost in complexities that are of secondary importance with respect to the flutter control problem and to reduce the problem to its bare essentials. One step toward accomplishing this was to concentrate primarily on the two structural modes that participate directly in the flutter and on the SISO zeros in the same frequency range which result from the choice of a particular sensor pair and control surface pair. Vibration modes dominated by sting deflections and their associated zeros were ignored, as were high-frequency modes. This procedure was possible because of effective pole/zero cancellations associated with the chosen control surfaces and sensors and because of frequency separation between the flutter dynamics and high-frequency modes.

Selection of sensors and control surfaces was a necessary first step in the controller design. The accelerometer pair at the TIP locations was chosen because this pair was responsive to the flutter motion and least responsive to high-frequency modes. The fourth-order 100-Hz Butterworth filter was used in the controller design and analysis. The TEO control surface pair was chosen because it was the most effective in controlling flutter. The TEI control surface pair was added later in the antisymmetric control law to improve stability margins. The design plant and final controller structure are shown in figure 6. In equation form, the controller was

$$\boldsymbol{\delta}_c = \mathbf{K}_1(s)\,\ddot{z}_{\text{TIP}}$$

$$= \begin{bmatrix} d \\ 1 \end{bmatrix} k_1 \frac{s}{s+a}\,\frac{s^2 + 2\zeta_N\omega_N s + \omega_N^2}{s^2 + 2\zeta_D\omega_D s + \omega_D^2}\,\ddot{z}_{\text{TIP}} \qquad (1)$$

where

$$\boldsymbol{\delta}_c = \begin{bmatrix} \delta_{\text{TEI}_c} \\ \delta_{\text{TEO}_c} \end{bmatrix}$$

The symmetric law was SISO. (The switch shown in fig. 6 was open.) All parameters in the controller were the same for both symmetries, and they have been specified numerically in the appendix. The term $\mathbf{K}_1(s)$ was implemented digitally for testing in the TDT.

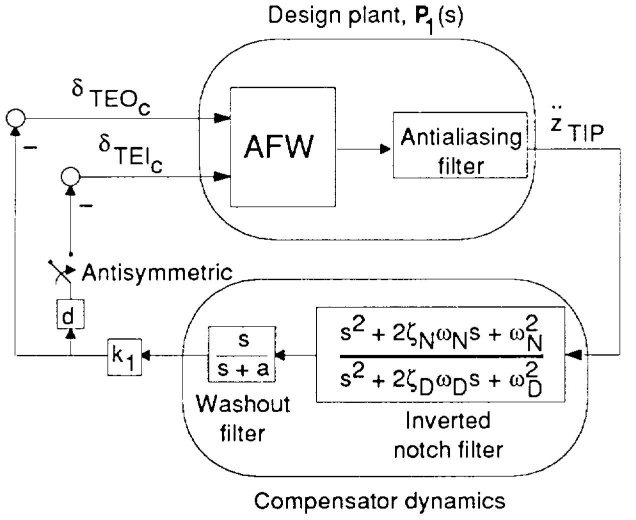

Figure 6. Block diagram of traditional pole/zero loci control law.

The steps to arrive at this controller form are presented subsequently. Note in figure 6 that the commands sent to the TEO and TEI surfaces in the antisymmetric case were dynamically equivalent in that they differed only by the constant factor ($d$). SISO design and analysis techniques were employed despite the possibility, for the antisymmetric law, that the resulting robustness characterization was nonconservative.

Straight feedback with no dynamic compensation was investigated first for an SISO design using the TIP accelerometer pair and the TEO control surface pair to see whether this feedback would be sufficient to stabilize the system, and if not, what problems would be encountered when attempting to employ a simple solution. Consideration of the high gain that was required and the desire to ensure a favorable root locus path led to the use of a second-order inverted notch filter to be described later in this section. A final consideration was that the response of the system to steady-state bias errors must be acceptably small; this consideration led to the addition of a first-order washout filter and resulted in a third-order controller.

***Critical zero.*** For the sketches of poles and zeros presented in figure 7, the horizontal axis was greatly exaggerated relative to the vertical axis to show more detail. All poles and zeros not associated with the compensator should be considered to lie near the imaginary axis. The sketch in figure 7(a) shows the loci of poles and zeros as functions of dynamic pressure. The poles are those associated with the two strongly interacting modes for the AFW wind-tunnel model with no active compensation, and the zeros arise from a particular choice of sensors and actuators. The pair of superimposed zeros at the origin results from the fact that accelerometers were used for feedback. A critical zero closely associated with the higher frequency of the two interacting modes was found for the TEO control surface and the TIP sensor. As dynamic pressure increased, the critical zero and the pole associated with the higher frequency mode stayed near each other until just below the flutter dynamic pressure at which point the pole broke away to the right and crossed into the unstable, right half of the complex plane.

The use of simple feedback will drive the closed-loop roots from the open-loop poles to the transfer function zeros as a function of feedback gain. However, given uncertainties in the model of the plant, it is not always clear what path the roots will take (ref. 27). Figure 7(b) shows how the system might be stabilized by simple feedback; figure 7(c) shows a case in which no value of feedback gain exists for which the closed-loop system will be stable.

Even when the desired path is followed, the location of the critical zero near the imaginary axis indicates that a high gain would be required to drive the unstable root close to the zero to stabilize the system. One difficulty associated with high-gain controllers is that the control surface rates required to control flutter while subject to continual turbulence excitation would be large and might saturate the rate capability of the actuators, thus causing a loss of flutter control. Another difficulty associated with high-gain

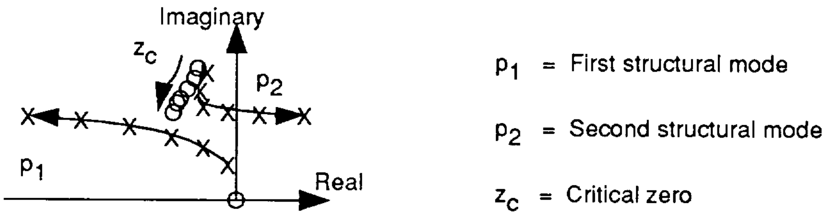

(a) Open-loop poles and zeros as function of dynamic pressure.

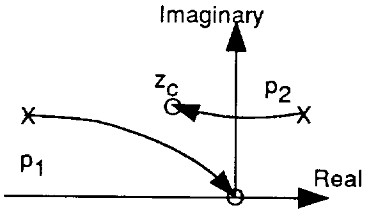

(b) Stabilizing feedback gain loci.

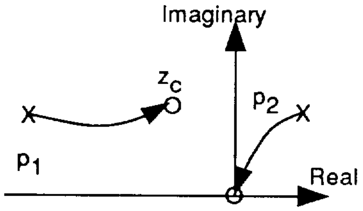

(c) Nonstabilizing feedback gain loci.

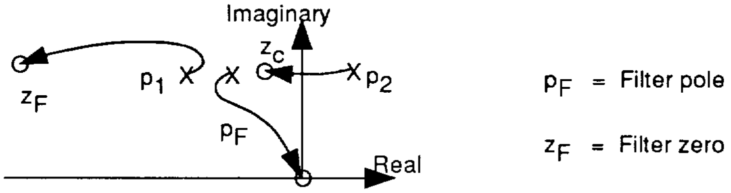

(d) Stabilizing dynamic feedback gain loci.

Figure 7. Sketch of pole/zero loci. Arrows indicate direction of increase in either dynamic pressure or gain.

controllers is that high-frequency modes or actuator roots can be driven to be unstable (ref. 53).

***Inverted notch filter.*** Dynamic filtering was required to reduce the feedback gain required for stabilization because of the location of the critical zero near the imaginary axis. The intent for this control law was to "soften" the effect of the critical zero by placing a filter pole near the critical zero and placing a filter zero farther to the left, as shown in figure 7(d). The result is similar to an inverted notch.

The location of the critical zero changes as a function of dynamic pressure, whereas the location of the open-loop filter pole is independent of dynamic pressure unless scheduling of controller dynamic parameters is used. Also, the actual locations of system zeros are difficult to predict analytically and can be difficult to measure experimentally. To avoid scheduling and because of the uncertainty about the exact location of the critical zero, the filter pole was placed somewhat to the left of the predicted critical zero and had a damping ratio of approximately 10 percent. This placement assured that the resulting pole-zero interaction would cause the desired stabilizing root-locus path to be achieved, even when subjected to moderate plant variations and modeling errors. Using frequency domain Nyquist criteria for stability margin analysis, a 50-percent damping ratio at a natural frequency 20 percent higher than that for the compensator pole was chosen for the compensator zero. This zero choice was made to simultaneously maximize the gain and phase margins of the system over a range of dynamic pressures.

Figure 8 shows the magnitude and phase plots of the frequency response of the inverted notch filter. The filter amplifies the control surface activity in the frequency range predicted for flutter, which in this case is approximately 11.5 Hz. Because the control surface activity was concentrated at this frequency, the controller made efficient use of the available control power and was fairly insensitive to modeling errors outside the frequency range of interest.

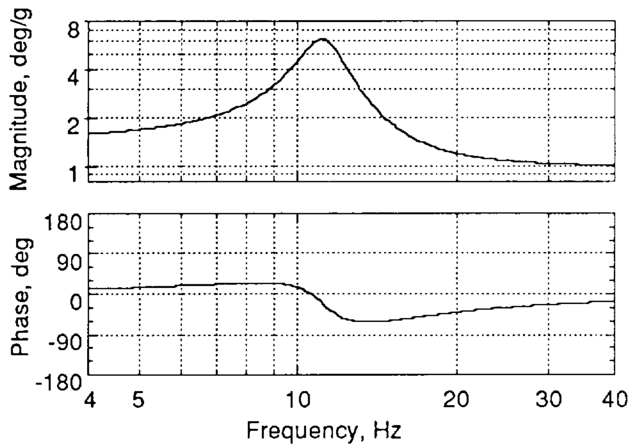

Figure 8. Frequency response for inverted notch filter in pole/zero loci control law.

It is generally thought that successful designs using pole/zero cancellation require an accurate knowledge of the plant; however, the inverted notch filter was evaluated using variations in the model of the AFW. The control law was judged to be tolerant to changes in the frequency of the flutter mode, and this tolerance was due in part to the robust placement of the filter pole with respect to the critical zero. The result was that the stabilizing character of the root locus did not change despite the frequency shifts.

The numerical values of the controller parameters in the continuous domain are presented in the appendix. The controller was implemented digitally by using a Tustin transformation and a 200-Hz sample rate. The design plant employed by the pole/zero loci methodology did not account for the time delays that resulted because of the digital implementation (see fig. 6). A "buy-back" approach was implemented, however, which approximately removed the effect of the 1 time step delay that was a result of the way the control law was implemented in the digital computer. The controller implementation was such that the controller output, which was computed based on sensor inputs and states at time $t_k$, was not sent out until $t_{(k+1)}$. The buy-back procedure follows. The discrete state equations for the controller resulting from the Tustin transformation were

$$\left.\begin{aligned} \mathbf{x}_{(k+1)} &= \mathbf{F}_d\mathbf{x}_k + \mathbf{G}_d\mathbf{y}_k \\ \mathbf{u}_k &= \mathbf{H}_d\mathbf{x}_k + \mathbf{E}_d\mathbf{y}_k \end{aligned}\right\} \qquad (2)$$

or, at $t_{(k+1)}$

$$\mathbf{u}_{(k+1)} = \mathbf{H}_d\mathbf{x}_{(k+1)} + \mathbf{E}_d\mathbf{y}_{(k+1)}$$

Because of the time delay in sending out the control command, the following was implemented if the buy-back procedure was not employed:

$$\mathbf{u}_{(k+1)} = \mathbf{H}_d\mathbf{x}_k + \mathbf{E}_d\mathbf{y}_k$$

In the buy-back procedure, the designer replaces $\mathbf{H}_d$ with $\mathbf{H}'_d = \mathbf{H}_d\mathbf{F}_d$ and $\mathbf{E}_d$ with $\mathbf{E}'_d = (\mathbf{H}_d\mathbf{G}_d + \mathbf{E}_d)$ in the implemented equation and makes the approximation that $\mathbf{y}_k \approx \mathbf{y}_{(k+1)}$. One obtains

$$\begin{aligned} \mathbf{u}_{(k+1)} &= \mathbf{H}'_d\mathbf{x}_k + \mathbf{E}'_d\mathbf{y}_k \\ &= \mathbf{H}_d\mathbf{x}_{(k+1)} + \mathbf{E}_d\mathbf{y}_k \\ &\approx \mathbf{H}_d\mathbf{x}_{(k+1)} + \mathbf{E}_d\mathbf{y}_{(k+1)} \end{aligned} \qquad (3)$$

The smaller that $\mathbf{E}_d\mathbf{y}_{(k+1)}$ and $\mathbf{E}_d\mathbf{y}_k$ are (relative to $\mathbf{H}_d\mathbf{x}_{(k+1)}$) the better the approximation. The approximation is exact if $\mathbf{E}_d = 0$. The lead introduced provides an approximate buy-back of the one-step computational delay.

***Predicted performance.*** The traditional pole/zero loci design was predicted through linear analysis and batch simulation to provide closed-loop stability up to the limit of the wind-tunnel operating range, as summarized in column two of table I. The term $q_{\max}$ refers to the maximum dynamic pressure, measured in pounds per square foot, for which the closed-loop system was predicted to be stable.

Table I. Predicted Performance for Traditional Pole/Zero Loci Design

| | | Margins at 300 psf | | rms control activity at 300 psf (percent of max allowed) | |
|---|---|---|---|---|---|
| Degrees of freedom | $q_{\max}$, psf | Gain, dB | Phase, deg | TEO, percent | TEI, percent |
| Symmetric | >350 | ±7 | ±33 | 73 | 3 |
| Antisymmetric | >350 | ±7 | ±38 | | |

A common evaluation point of 300 psf was chosen for each of the control laws. The gain and phase margins for the pole/zero design were predicted through linear analysis to exceed the design requirements at 300 psf. Other analyses, not shown, predicted that the margins were maintained throughout the test envelope. Positive and negative gain margins were verified in the batch simulation at selected dynamic pressures by individual variation of symmetric and antisymmetric gains until simulation time histories exhibited oscillatory divergence. Phase margins were more difficult to verify in the batch simulation, and only tolerance to phase lag was investigated. This investigation was accomplished by incrementally reducing the break frequency of the fourth-order Butterworth filter from the nominal value of 100 Hz until the simulation time histories showed oscillatory divergence. The tolerance to phase lag was equated to the additional phase lag because of the break frequency reduction at the frequency of divergent oscillation.

The rms control activity in table I is shown in terms of a percent of the maximum acceptable rms rate of 75 deg/sec. The predicted requirements are well within their limits, and the TEO surfaces are the dominant ones used for flutter suppression. These results have been generated using the batch simulation in the presence of simultaneous symmetric and antisymmetric turbulence excitation.

Analyses were made which predicted that the pole/zero loci control law structure was robust to variations in the plant. In these analyses, an early version of the inverted notch filter was employed for which the compensator zero was more heavily damped ($\zeta_N = 0.707$) than that ultimately selected ($\zeta_N = 0.47$). The robustness characteristics, to be described, hold for both choices; the primary reason for the ultimate choice of the less-damped zero was to simultaneously maximize the gain and phase margins of the system over a range of dynamic pressures. Cases were examined with the SISO form (the switch shown in fig. 6 was open) with both symmetries; and cases were examined with the MISO form (the switch was closed). Each version of the controller stabilized the plant to a dynamic pressure of 325 psf or more under the following simulated conditions: a Mach number of 0.5 in air, a Mach number of 0.8 in a heavy gas test medium, and a Mach number of 0.9 in a heavy gas test medium. Because the controller stabilized these varieties of plants, there was confidence that wind-tunnel testing of the pole/zero loci controller would be successful.

## Modal Rate Feedback Design (Design Number 2)

***Overview.*** The design philosophy for the modal rate feedback control law was to use linear combinations of multiple accelerometer signals and dynamic compensation to synthesize the flutter mode rate for feedback to multiple control surfaces (refs. 11, 19, and 25). The control structure used is shown in figure 9. A 1.5 time step delay was included in the design plant to account for the effects of a digital implementation of a continuous controller. Consequently, the continuous controller had a 1.5 time step lead to counterbalance the digital implementation delay. The first-order 25-Hz antialiasing filters were selected for analysis and design. Numerical values determined for the controller parameters are presented in the appendix. Multiple sensors were used to identify the activity of the flutter mode not only by frequency but also by the geometry of its characteristic mode shape. Multiple control surfaces were used to control the flutter mode without affecting other modes. Isolation of the flutter mode was determined by the filtering included in the design plant, the compensator dynamics, and the extent to which the blending and distributing rejected feedback interaction with other modes.

***Control structure definition.*** The blending coefficients used for the accelerometer pairs, the distribution coefficients used for the control surface pairs, and the overall system gain were the design variables used in an optimization procedure. The ordering of the four pairs of sensors used was

$$\ddot{\mathbf{z}} = \begin{bmatrix} \ddot{z}_{\mathrm{LEO}} \\ \ddot{z}_{\mathrm{TEI}} \\ \ddot{z}_{\mathrm{TEO}} \\ \ddot{z}_{\mathrm{TIP}} \end{bmatrix}$$

and the ordering of the two pairs of control surfaces used was

$$\boldsymbol{\delta}_c = \begin{bmatrix} \delta_{\mathrm{TEI}_c} \\ \delta_{\mathrm{TEO}_c} \end{bmatrix}$$

In equation form, the control law was

$$\begin{aligned} \boldsymbol{\delta}_c &= \mathbf{K}_2(s)\,\ddot{\mathbf{z}} \\ &= \mathbf{D}_{\mathrm{IS}} k_2 \mathbf{T}_2(s)\,\mathbf{B}_{\mathrm{LN}}\ddot{\mathbf{z}} \qquad (4) \end{aligned}$$

The controller $\mathbf{K}_2(s)$ was implemented digitally for testing in the TDT.

The controller dynamics $\mathbf{T}_2(s)$ were chosen by the control law designer. In the flutter frequency

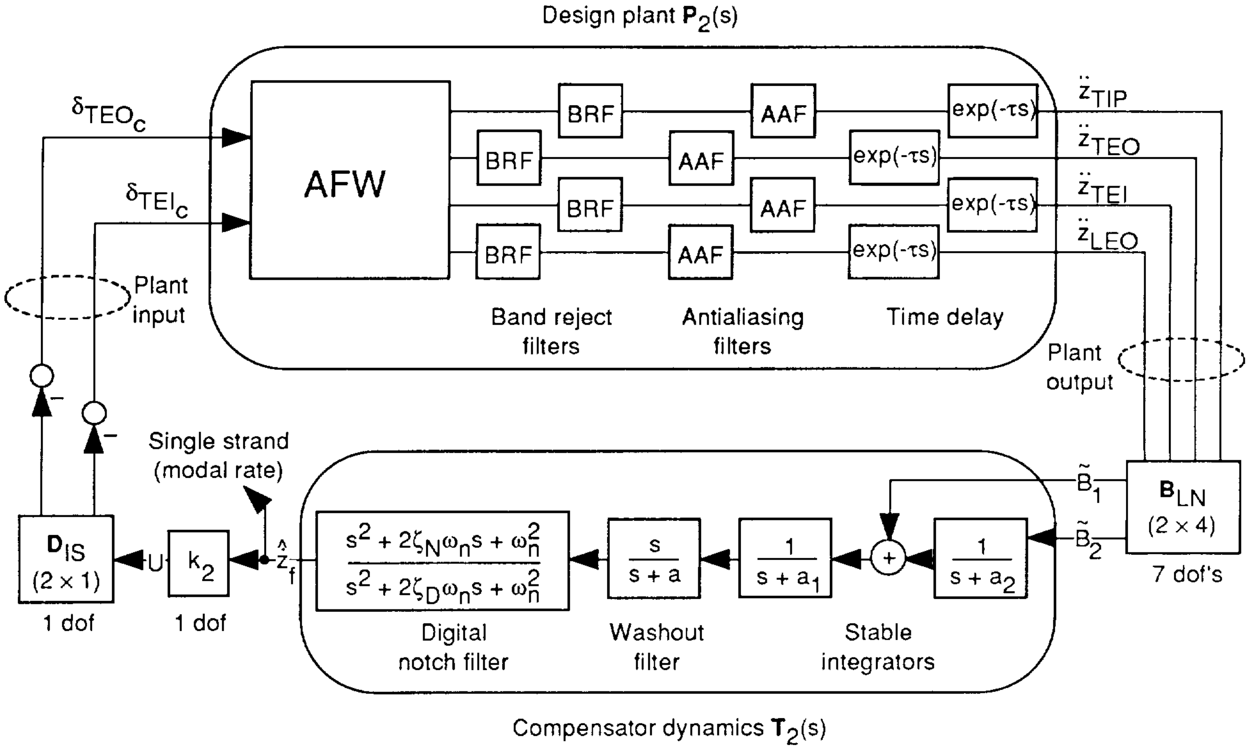
Design plant $\mathbf{P}_2(s)$
$\delta_{TEO_c}$
$\delta_{TEI_c}$
AFW
BRF
AAF
exp(-τs)
$\ddot{z}_{TIP}$
$\ddot{z}_{TEO}$
$\ddot{z}_{TEI}$
$\ddot{z}_{LEO}$
Band reject filters
Antialiasing filters
Time delay
Plant input
Plant output
Single strand (modal rate)
$\tilde{B}_1$
$\tilde{B}_2$
$\mathbf{B}_{LN}$ (2 × 4)
7 dof's
$\mathbf{D}_{IS}$ (2 × 1)
1 dof
U
$k_2$
1 dof
$\hat{\dot{z}}_f$
$\frac{s^2 + 2\zeta_N\omega_n s + \omega_n^2}{s^2 + 2\zeta_D\omega_n s + \omega_n^2}$
$\frac{s}{s+a}$
$\frac{1}{s+a_1}$
+
$\frac{1}{s+a_2}$
Digital notch filter
Washout filter
Stable integrators
Compensator dynamics $\mathbf{T}_2(s)$

Figure 9. Block diagram of modal rate feedback control law.

range, rate and position components are included in the single-strand signal by passing signals $\tilde{B}_1$ and $\tilde{B}_2$ through one and two integrations, respectively. Low-pass filter elements having break frequencies that were low relative to the flutter frequency, referred to here as stable integrators, were used in lieu of pure integrators to avoid potential high-gain difficulties with sensor bias and quantization effects. The second stable integrator (position path) was included to allow more freedom to change the phasing of individual sensor channels. A first-order "washout" filter with a zero at the origin and a pole at a frequency below the flutter frequency was also used to reduce response to bias errors and low-frequency disturbances. Finally, a second-order notch filter, which was ultimately implemented digitally, was used to adjust the phasing of the control action at the flutter frequency and to reduce the response to a nonflutter mode. The notch for the symmetric case was for a 5.7-Hz sting mode, and the notch for the antisymmetric case was for an 18.3-Hz structural mode.

Coefficients and parameter values are shown in the appendix; the process by which the design variables were determined will be described. When examining the blending coefficients, note that the integrators attenuate a signal proportional to the frequency of the signal. Therefore, to more readily compare the contributions of individual sensors used in feedback, each row of the blending coefficient matrix was separated into a multiplicative factor and that row normalized by the factor. The normalizing factor chosen for the first row (one integration) was 70 rad/sec (11.14 Hz), which is a number close to the predicted flutter frequency. The normalizing factor chosen for the second row (two integrations) was the square of that for the first row.

The method compares the predicted and a reference desired response during the optimization. Thus, for each symmetry, individual frequency responses were required for each (accelerometer pair/actuator pair). These responses can be obtained either through pretest modeling or through experiment as was done successfully in reference 54. Analytical frequency responses were generated using the ISAC system of programs (ref. 45). The responses were computed using the nonstate-space form of the equations of motion, thus removing the need to make rational function approximations of the unsteady aerodynamic forces. Experimentally derived frequency responses, which were also used during the wind-tunnel entry to improve the control law, will be discussed subsequently.

***Flow diagram.*** The signals designated in figure 9 as $\delta_c$ and $\ddot{\mathbf{z}}$ represent, respectively, commanded control surface deflections and measured local accelerations for a given symmetry. The frequency response for each acceleration signal resulting from each control surface command (either symmetric or antisymmetric) for continuous analytical models of the AFW wind-tunnel model was precomputed for the frequency range from 2 Hz to 64 Hz; these computations were repeated for several dynamic pressures and the frequency responses were retained for further analysis. For the purpose of control law design (performed in the continuous domain), frequency responses representing the effects of the time delays (a $1.5T$ delay was assumed) and of a candidate set of analog antialiasing and notch filters were also computed and combined with the frequency responses that represented the AFW wind-tunnel model. This design plant model was used in the development of the control law. Frequency responses representing the two paths through the controller dynamics were also precomputed and stored in combination with frequency responses for the design plant. This process reduced the amount of time required for each iteration of the optimization.

***Optimization strategy.*** Although the normalized blending and distribution matrices contained eight and two coefficients, respectively, the magnitude of the largest coefficient of each matrix was factored into a system gain. Thus, these matrices had seven and one degrees of freedom, respectively, which, together with the system gain, constituted the nine available degrees of freedom (identified in fig. 9) for use as design variables in the optimization procedure.

The output from the dynamic compensator was a single-strand point for the feedback path. The optimizer was used to drive the composite frequency response at that point to match a simple, desired frequency response $R(s)$ (see eq. (6)), which was proportional to the idealized modal rate of the flutter mode, generated from a continuous state-space model of the AFW. Thus, the desired frequency response was proportional to that of the rate of a simple oscillator with damping ratio $\zeta_f$. At the design point chosen, 325 psf, this oscillator was unstable. Figure 10 illustrates the concept of feedback of modal rate to add damping. The value of the gain ($k$) was chosen to be $|4\zeta_f|$ where the damping ratio was that predicted for the design point of 325 psf. For an unstable plant, this choice of gain corresponds to what would be found for the minimum energy stabilizing controller.

Figure 11 shows Nyquist (or polar) plots of the predicted $T_{SS}(s)$ and desired $R(s)$ loop-transfer-function frequency responses, as defined at the single-strand point (see fig. 9 and eqs. (5) and (6)):

$$T_{SS}(s) = \mathbf{T}_2(s)\,\mathbf{B}_{LN}\mathbf{P}_2(s)\,\mathbf{D}_{IS}k_2 \tag{5}$$

and

$$R(s) = \frac{k\omega_f s}{s^2 + 2\zeta_f\omega_f s + \omega_f^2} \tag{6}$$

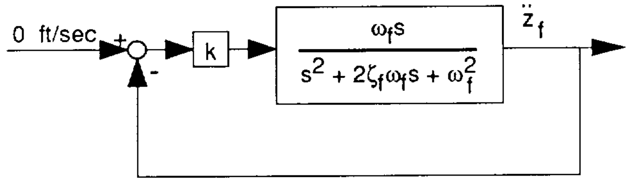

Figure 10. Block diagram of rate feedback.

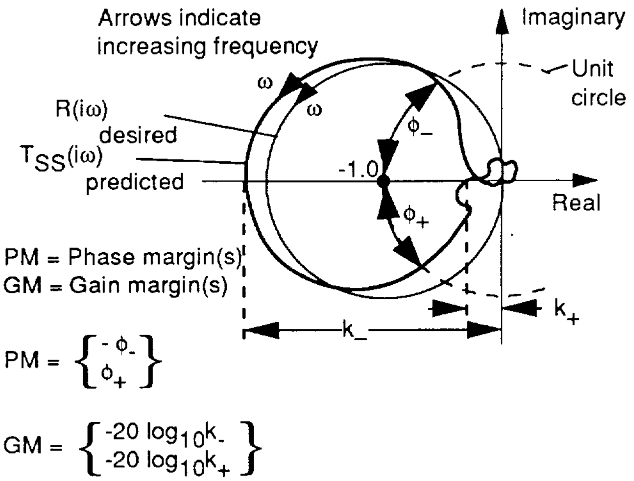

Figure 11. Predicted and desired single-strand loop transfer function; antisymmetric, 325-psf condition.

The frequencies used in the analysis range from 2 Hz to 64 Hz. A full Nyquist plot would span frequencies from minus infinity to plus infinity and be a symmetric function of frequency (with respect to the real axis) so that the depiction of the negative frequency portion would be redundant. The Nyquist stability criterion requires that, for each unstable pole of the open-loop system, the Nyquist plot must form one counterclockwise encirclement of the $-1$ point in order for the closed-loop system to be stable. For oscillatory instabilities, the unstable poles occur in complex conjugate pairs, thus requiring two encirclements per pair. However, one of the encirclements would occur for the frequency range from minus infinity to zero, which is not shown. Figure 11 represents a condition considerably above the predicted flutter dynamic pressure, and the counterclockwise encirclement of the $-1$ point indicates that the unstable flutter mode would be stabilized through feedback.

For actively stabilized flutter, the encirclements will occur in the vicinity of the flutter frequency. Gain and phase margins, with respect to errors at the single-strand point, can be read directly from a Nyquist plot (as indicated in fig. 11) as the amount of shift that can be tolerated while still encircling the $-1$ point. Errors that contribute to excess phase lag at the flutter frequency will shift the positive frequency plot clockwise (and the negative frequency plot counterclockwise) until closed-loop instability is encountered at a frequency slightly above the flutter frequency. Similarly, errors that contribute to excess phase lead result in closed-loop instability at a frequency slightly below the flutter frequency.

The response of modes other than the flutter mode will be evident as additional "lobes" on the Nyquist plot. To the extent that the sensor and control surface blending can isolate the flutter mode, these extra lobes will be small. If these lobes are not small, they could result in clockwise encirclements of the $-1$ point, thus indicating that an open-loop-stable mode would be driven unstable, through feedback, at a frequency other than the flutter frequency.

The cost function for the optimization contains the sum of the squares of the difference between the predicted and the desired response, multiplied by frequency dependent weights, together with penalty contributions for rms actuator rate violations; this function is shown in equation (7):

$$J = \sum_{n=1}^{n_\omega} W_{\omega_n} \left[T_{\mathrm{SS}}(i\omega_n) - R(i\omega_n)\right] \mathrm{conj}\left[T_{\mathrm{SS}}(i\omega_n) - R(i\omega_n)\right] + \sum_{m=1}^{m_\delta} W_{\delta_m} \left\{ \max\left[0, \left(\dot{\delta}_{m_c}\right)_{\mathrm{rms}} - \overline{\left(\dot{\delta}_{m_c}\right)_{\mathrm{rms}}} \right] \right\}^2 \tag{7}$$

where $R(i\omega_n)$ is the desired modal rate feedback frequency response at the $n$th frequency; $T_{\mathrm{SS}}(i\omega_n)$ is the analytically achieved single-strand frequency response at the $n$th frequency; $W_{\omega_n}$ is the weight defining the cost of error between desired and achieved single-strand frequency responses at the $n$th frequency; $\overline{(\dot{\delta}_{m_c})_{\mathrm{rms}}}$ is the maximum allowable commanded rms rate for the $m$th actuator; $(\dot{\delta}_{m_c})_{\mathrm{rms}}$ is the commanded closed-loop rms control rate in response to turbulence for the $m$th actuator; and $W_{\delta_m}$ is the weight penalty for violating the $m$th constraint. To the extent that the actual response matches the desired response, the system, as observed at the single-strand point, will behave as though it had rate feedback for adding damping to the unstable flutter mode.

A Davidon-Fletcher-Powell optimization routine (ref. 55) was used to find the system gain and blending and distribution matrix coefficients for which the cost function was minimized at a particular dynamic pressure. Each resulting design was evaluated at other dynamic pressures. Predicted performance was satisfactory throughout the wind-tunnel test envelope.

Several schemes for selecting the frequency-dependent weights were considered. Initially, the weights were chosen to more heavily penalize the errors in a discrete band about the flutter frequency than those outside the discrete band. Alternately, the weights were chosen which were proportional to the magnitude of the desired response, thus again most heavily penalizing errors at the center frequency of the flutter mode. Uniform weighting across a linear distribution of all available frequencies, from 2 Hz to 64 Hz, was also used. The weighting used for the final analytically and experimentally derived control laws was uniform on a logarithmic frequency scale, which penalized low-frequency errors more heavily than high-frequency errors compared with the linear frequency distribution. The uniform weighting (on a logarithmic scale) scheme exploits sensor blending and control distribution in the low-frequency range where the model is expected to be more accurate. The scheme requires reliance, instead, upon dynamic filtering to attenuate model response at high frequencies where the analytical model is less well-known. In practice, achievement of the desired Nyquist plot for the single-strand point was not particularly sensitive to the weighting scheme chosen. Throughout the design process, the initial part of an optimization run would capture the bulk of the achievable Nyquist plot shaping at the single-strand point, with only limited and very slow improvement in the cost function (and Nyquist plot) as the optimization was allowed to continue. However, none of the convergence criteria were achieved, and the values of the blending and distribution coefficients changed over time, thus suggesting that multiple combinations of coefficients existed which would generate approximately the same single-strand Nyquist plot and cost function value. Additional discussion of problems with this approach will be presented in the section entitled "Posttest Analysis."

At all times during the optimization process, the distribution coefficient for the TEO surface was larger in magnitude than the distribution coefficient for the TEI surface. At some times, the coefficient for the TEI surface had a sign opposite to the sign of the coefficient for the TEO surface. Opposing signs are reasonable for a condition in which a node line for the flutter mode is located between the two control surfaces. However, the closed-loop rms control rate because of turbulence for the TEO surface was found to be higher for a suboptimal solution with opposing signs than for a suboptimal solution with like signs for the two surfaces. The opposition of signs occurred after a lengthy optimization cycle that only slightly improved the cost function and the single-strand Nyquist plot. (The rms control rate constraints were not active at this time.) Because of concern that the two surfaces might be "working against each other," the sign of the TEI surface was forced to match the sign of the TEO surface, and the magnitude of the coefficient for the TEI surface was set to a value that reduced the rms activity of the TEO surface. This procedure removed one degree of freedom in the optimization.

***Control surface rates.*** Figure 12 shows the predicted power spectral density (PSD) plots at a dynamic pressure above the open-loop flutter point for symmetric closed-loop rates for the TEO and TEI control surfaces caused by the modeled turbulence. (A 1-ft/sec rms, symmetric gust velocity was assumed.) These plots are representative examples that illustrate the removal of undesirable high-frequency actuator commands; they do not depict the PSD for a control law actually tested. The control surface rms rate in deg/sec can be calculated as the square root of the integral with respect to the frequency of the PSD. The design limit for the total control surface activity was chosen to be 75 deg/sec, as discussed earlier.

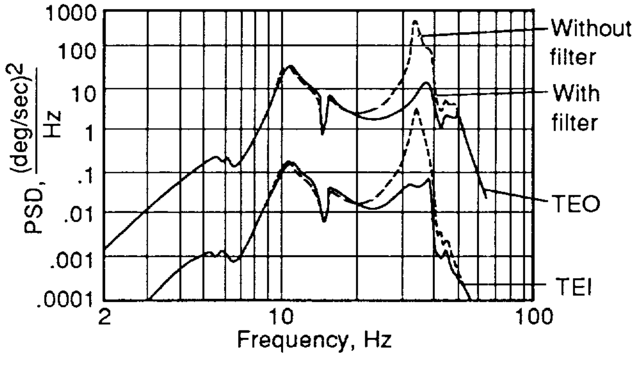

Figure 12. Predicted, control-surface-rate power spectral density caused by unit rms gust; closed-loop, symmetric, 300-psf condition.

A peak can be seen in the control surface activity at a frequency of approximately 11.5 Hz. This peak represents the activity required to suppress the critical, stabilized, flutter mode as it is excited by turbulence. The figure also shows significant undesirable control surface activity in the 25-Hz to 40-Hz frequency range; this activity results from turbulence excitation of high-frequency structural modes. An analog band-rejection filter was used to reduce control surface activity in this region. This filter consisted of three fairly broad second-order notches with center frequencies at 32 Hz, 40 Hz, and 49 Hz. The form of the individual notch elements making up the band-rejection filter is shown below:

$$\mathrm{BRF} = N_1 N_2 N_3 \tag{8}$$

where

$$N_j = \frac{s^2 + 2\zeta_{N_j}\omega_{n_j}s + \omega_{n_j}^2}{s^2 + 2\zeta_{D_j}\omega_{n_j}s + \omega_{n_j}^2}$$

Numerical values for the notch filter parameters are shown in the appendix. The band-rejection filter was used instead of a low-pass filter to keep the resulting lag at the flutter frequency to a minimum, while still achieving the desired attenuation. The lag at 11.5 Hz, which was due to the filter, was approximately 28°. Both table II and figure 12 show that the band-rejection filter attenuates a significant portion of the undesired high-frequency commands to the control surfaces in the 30-Hz to 40-Hz range. Prior to the use of the band-rejection filter, the rms control rate constraints were violated, and they actively contributed to the cost function evaluation used in the optimization. After the band-rejection filter was designed and incorporated into the design plant, the rms control rate constraints no longer contributed to the cost function.

Table II. Predicted Control Rate Reduction With Band-Rejection Filter for Modal Rate Feedback Design

[300-psf condition]

| rms rates | Without filter, deg/sec | With filter, deg/sec |
|---|---|---|
| TEO | 138 | 52 |
| TEI | 11 | 4 |

See the appendix for the values chosen for parameters in the dynamic compensation, the distribution matrices ultimately selected, and the blending matrices found by the optimization procedure.

***Predicted performance.*** Table III shows the predicted performance for the modal rate feedback controller which resulted from linear analysis and which was substantially confirmed by nonlinear batch simulation. Both the symmetric and the antisymmetric control laws were predicted to stabilize the closed-loop system over the TDT test path to the tunnel limit. The gain and phase margins are shown, with respect to errors at the single-strand point, at the common evaluation point of 300 psf. These gain and phase margins were predicted by linear analysis to meet the stated requirements throughout the wind-tunnel test envelope. The gain margins were verified in simulation, at selected dynamic pressures, by varying symmetric and antisymmetric system gains individually until simulation time histories showed divergence. These gain margins obtained from simulation were comparable to those obtained through linear analysis. The phase margins were not verified through batch simulation.

Table III. Predicted Performance for Modal Rate Feedback Design

| | | Margins at 300 psf | | rms control activity at 300 psf (percent of max allowed) | |
|---|---|---|---|---|---|
| Degrees of freedom | $q_{\max}$, psf | Gain, dB | Phase, deg | TEO, percent | TEI, percent |
| Symmetric | >325 | ±9 | ±34 | 67 | 25 |
| Antisymmetric | >325 | ±12 | ±49 | | |

The predicted rms control surface rate was determined by using the batch simulation with simultaneous symmetric and antisymmetric turbulence excitation. The simulation indicated that the specified rms control surface rate limit was not exceeded for either pair of control surfaces. Significant activity was commanded for both the TEO and the TEI surfaces, although the TEO surfaces dominated.

### Modified LQG Design (Design Number 3)

***Overview.*** Initial symmetric and antisymmetric control laws were designed using a modified LQG procedure. The philosophy behind this control law design was to obtain a minimum energy, full-order, optimal controller consisting of a linear quadratic regulator and a model-based Kalman state estimator for output feedback and then to reduce its order without significant loss of the full-order controller robustness and performance characteristics. The control law was then discretized for implementation.

Figure 13 shows the analog design plant that contained the basic state-space model augmented with antialiasing filters and a first-order Padé approximation for the digital controller 1 computational time step delay. The 25-Hz first-order antialiasing filters were selected for analysis and design. The TEO and LEO control surfaces were used for control input, and their collocated accelerometers were used as sensors for feedback. Washout filters were added to the control law after completion of the modified LQG design process. Analog notch filters were also added after the design to improve high-frequency robustness characteristics above 30 Hz. Numerical values for controller parameters are presented in the appendix. In equation form, that part of the control law which was implemented digitally is

$$\begin{aligned}\boldsymbol{\delta}_c &= \mathbf{K}_3(s)\,\ddot{\mathbf{z}}\\ &= \left[\frac{s}{s+a}\right]\left[\mathbf{H}\,(s\mathbf{I}-\mathbf{F})^{-1}\,\mathbf{G}+\mathbf{E}\right]\ddot{\mathbf{z}} \qquad (9)\end{aligned}$$

where

$$\boldsymbol{\delta}_c = \begin{bmatrix}\delta_{\mathrm{LEO}_c}\\ \delta_{\mathrm{TEO}_c}\end{bmatrix}$$

$$\ddot{\mathbf{z}} = \begin{bmatrix}\ddot{z}_{\mathrm{LEO}}\\ \ddot{z}_{\mathrm{TEO}}\end{bmatrix}$$

$$\dot{\mathbf{x}}_u = F\mathbf{x}_u + G\ddot{\mathbf{z}}$$

$$\boldsymbol{\delta}_c = H\mathbf{x}_u + E\ddot{\mathbf{z}}$$

***Design steps.*** The LQG design and order reduction was arrived at through the iterative procedure shown in figure 14. Two design points (dynamic pressures of 300 psf and 350 psf) were chosen where the design plant was unstable. The full-state feedback, optimal regulator for each symmetry and design point was designed with a zero weighting matrix for the states and an identity weighting matrix for the controls. For the closed-loop system, this regulator reflects the unstable plant characteristic roots into the left-half plane, while all other roots remain unchanged; this represents the minimal control energy solution for stabilizing the plant (ref. 56). The model-based Kalman state estimator was designed with a diagonal fictitious input noise intensity matrix with elements of 0.000001 rad$^2$, a gust input noise intensity of 1/144 (ft/sec)$^2$, and a diagonal measurement noise intensity matrix with elements of 1/144 (ft/sec$^2$)$^2$.

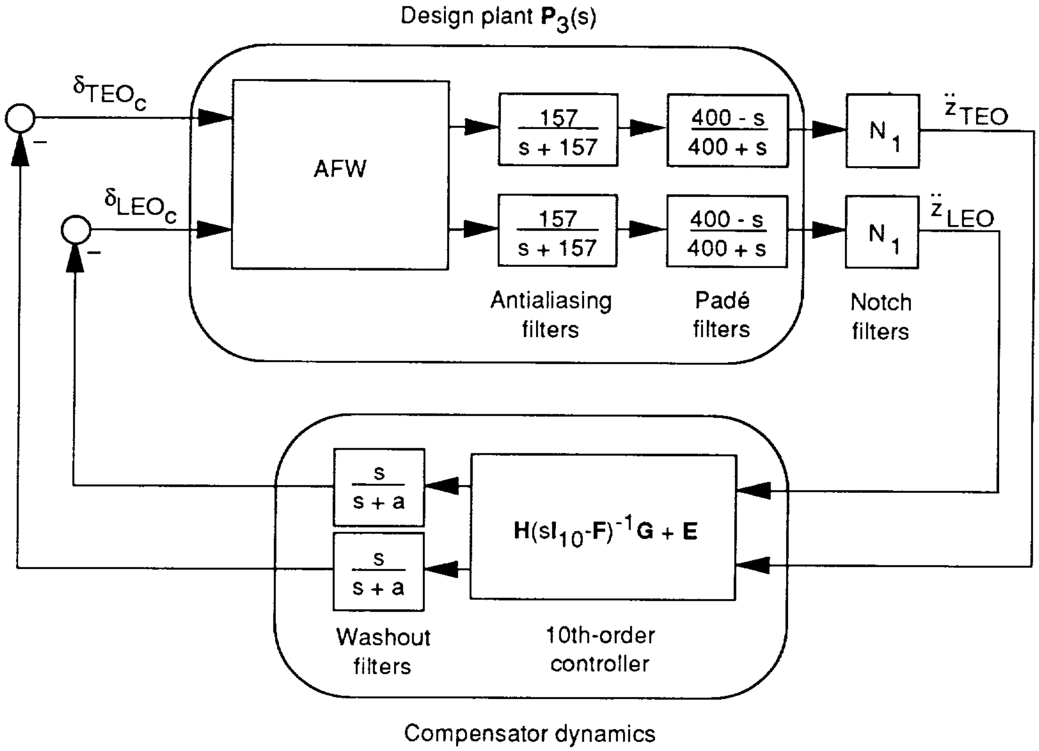
Design plant $P_3(s)$
$\delta_{TEO_C}$
$\delta_{LEO_C}$
AFW
$\frac{157}{s+157}$
$\frac{400-s}{400+s}$
$N_1$
$\ddot{z}_{TEO}$
$\ddot{z}_{LEO}$
Antialiasing filters
Padé filters
Notch filters
$\frac{s}{s+a}$
$H(sI_{10}-F)^{-1}G+E$
Washout filters
10th-order controller
Compensator dynamics

Figure 13. Block diagram of modified LQG control law.

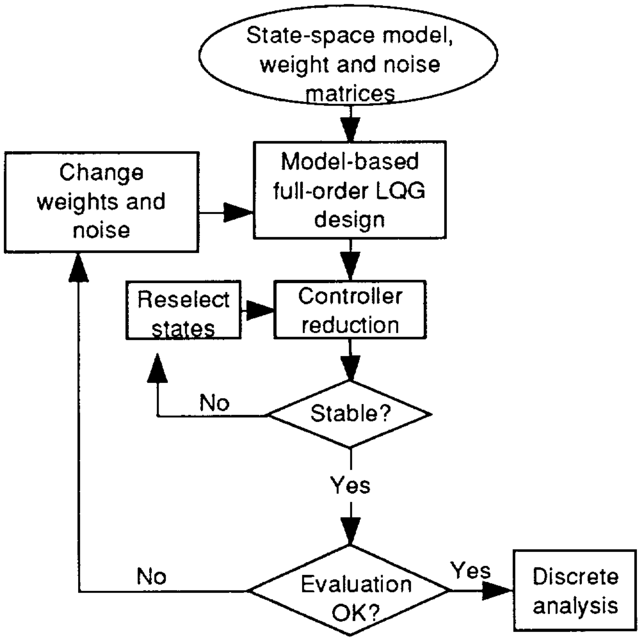
State-space model, weight and noise matrices
Change weights and noise
Model-based full-order LQG design
Reselect states
Controller reduction
No
Stable?
Yes
No
Evaluation OK?
Yes
Discrete analysis

Figure 14. Steps in modified LQG design process.

The full-state feedback regulator was combined with the state estimator to generate a full-order compensator that used only sensor feedback with no direct knowledge of the states of the plant. The resulting full-order controller required order reduction for implementation. The full-order LQG control law was reduced through a process of balanced realization and modal truncation, based in part upon the evaluation of modal residues (ref. 40). Controller poles above 25 Hz were removed because they had little effect on the control of flutter at 11.5 Hz. A 10th-order control law was chosen since its robustness and performance characteristics were close to those of the full-order LQG control law. The numerical values of the parameters in the continuous symmetric and antisymmetric control laws, designed for the 300-psf and 350-psf points, are shown in the appendix. First-order washout filters were added to attenuate the response to bias errors, which increased the controller order to 12. Additional singular value analysis revealed the need for stability margin improvement in the 32-Hz frequency range. Because the open-loop plant poles in this region are stable, signal attenuation by means of an analog notch filter (see eq. (8)) with a center frequency of 32 Hz was added to prevent the compensator from driving the modes to be unstable in this region.

The final step was to discretize the continuous control law at a sample rate of 200 samples per second using the Tustin transformation. With this transformation, the controller transfer matrix in the analog domain and that implemented in the digital

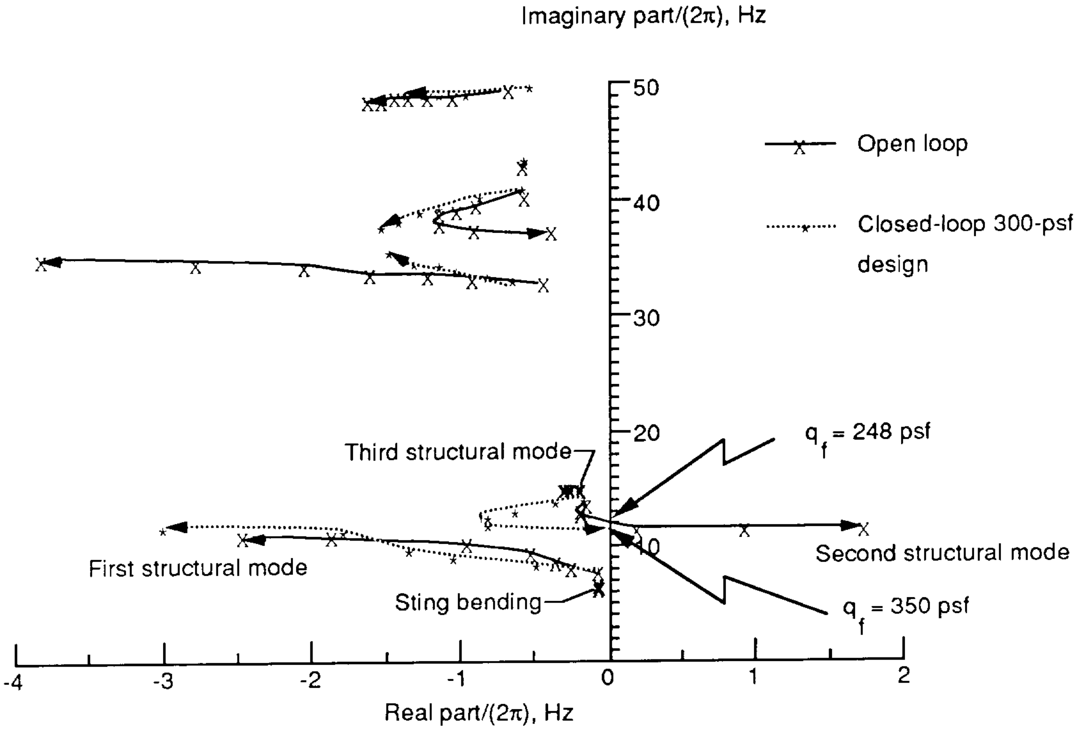

Figure 15. Predicted dynamic pressure root loci; symmetric condition; range is from 0 psf to 350 psf at 50-psf increments.

domain were virtually identical at and below the flutter frequency except for the 1.5 time step delay present in the digital implementation. The Padé approximation to the 1 time step delay that was included in the design plant (see fig. 13) resulted in a 1 time step lead in the continuous controller that counterbalanced 1 time step of the digital implementation delay.

***Poles as function of*** $q$. Figure 15 shows the predicted plant open-loop poles and predicted fixed-gain, closed-loop roots as functions of dynamic pressure for the symmetric degrees of freedom. The reduced-order 300-psf control law with washouts and 32-Hz notches was used. To simplify the figure, compensator poles and zeros are not shown. Compensator poles do not change with dynamic pressure when the feedback loops are open. When feedback loops are closed, the compensator poles interact with those of the plant and then change with dynamic pressure. However, for this design, the open- and closed-loop compensator poles are stable for the dynamic pressure range shown.

The solid lines in figure 15 indicate the paths of the open-loop poles, and the dashed lines indicate the paths of the closed-loop roots. The crossing point where the 11.5-Hz flutter mode becomes unstable is identified in the figure as 248 psf for the design model of the symmetric plant with no compensation and as 350 psf for the symmetric plant with compensation. The corresponding values for the antisymmetric flutter mode were 252 psf and 325 psf, respectively. (The root loci are not shown.)

***Predicted performance.*** The modified LQG control law based on the 300-psf design point was predicted through analysis and simulation to provide closed-loop stability to the limit of the wind-tunnel operating range. The gain and phase margins shown in table IV represent guaranteed minimum margins for simultaneous variations on multiple channels (ref. 57). These margins can be conservative if they represent an unlikely combination of variations. The margins shown here do not meet the requirements for SISO gain and phase margins. However, because of their potentially conservative nature, these margins were judged to be sufficient for testing the control law.

The closed-loop rms control surface rates in the presence of random gust excitation are within the specified limits. The percent of maximum allowed control surface activity for each pair of surfaces indicates that both the TEO and LEO control surface pairs are used to a significant extent, but the TEO surfaces are dominant. The rms control surface rates were generated with both symmetrics active by using the batch simulation. Separate linear analyses of rms control rate activity were performed for each

Table IV. Predicted Performance for Modified LQG Design

[Laws based on 300-psf design point]

| Degrees of freedom | $q_{\max}$, psf | Margins at 300 psf (at plant input)[a] |  | rms control activity at 300 psf (percent of max allowed) |  |
|---|---|---|---|---|---|
|  |  | Gain, dB | Phase, deg | TEO, percent | LEO, percent |
| Symmetric | 350 | ±3 | ±18 | 62 | 26 |
| Antisymmetric | 325 | ±4 | ±20 |  |  |

[a] Equivalent multivariable margins for simultaneous independent changes on all channels.

symmetry for the 300-psf controller. These analyses showed that, for a unit gust intensity, the antisymmetric control activity was only approximately 25 percent as large as the symmetric control activity.

## Wind-Tunnel Test Results

### Measured Versus Predicted AFW Wind-Tunnel Model Characteristics

A variety of information was collected during the test. Runs that were made early in the entry established that the uncontrolled flutter dynamic pressure of the decoupled tip ballast store configuration was sufficiently high to provide the desired flutter-stopper capability. This capability was achieved, however, only after adjusting the stiffness of the torsional spring that is activated in the decoupled configuration to avoid adverse coupling with model elastic modes of approximately 6 Hz. The stiffness was adjusted to reduce the frequency of a tip ballast store mode from 6 Hz to 4.5 Hz. The possibility of this requirement had been anticipated, and the stiffness adjustment capability had been built into the design.

Flutter clearance runs were made with the tip ballast stores in the coupled configuration to establish the uncontrolled flutter boundary for the configuration that was to be tested in a closed-loop manner. Differences were observed between predicted and actual flutter dynamic pressures. The dynamic pressure for antisymmetric flutter was found to be lower than that predicted by approximately 30 psf or 13 percent based upon a large, primarily antisymmetric response encountered at a dynamic pressure of about 220 psf. Analysis had indicated that symmetric flutter would occur first, at approximately 248 psf, with antisymmetric flutter occurring at about 252 psf.

Subcritical open-loop runs were made to obtain estimates of plant frequency response functions. In these runs, excitation was generated within the digital computer and sent out to an actuator pair as either a symmetric or an antisymmetric command. A sinusoidal excitation was input with the frequency varying logarithmically with time over a 150-sec period from 4 Hz to 35 Hz. The input and outputs of interest were recorded digitally and processed, in near real time, using fast Fourier transform techniques to obtain plant estimates. A key difference between predicted and actual characteristics was evident. For both symmetries, the frequencies at which dominant frequency response peaks occurred were somewhat lower than predicted. Figure 16(a), which shows the symmetric case at a dynamic pressure of 175 psf, contains a comparison of predicted and measured Bode plots of $\ddot{z}_{\mathrm{TIP}}/\delta_{\mathrm{TEO}_c}$. This sensor/control combination exhibits similarities and differences that are typical of what has been seen with other combinations. Both curves contain the effect of the antialiasing filters and a 0.5 time step delay. (The 1 time step delay associated with controller output commands is not present here.) The predicted and measured curves exhibit the same trend over the frequency range shown, and they show good agreement in peak magnitudes. However, a shift of approximately 1 Hz is evident in the frequency at which the peak occurs for the lower frequency of the two interacting modes. The analytical model had been adjusted so that the frequencies at zero dynamic pressure matched the frequencies measured during a ground vibration test. The differences between predicted and measured frequencies must, therefore, be related to aerodynamic effects that could arise from a number of sources, including errors in the predicted mode shapes.

The phase characteristics of the response shown in figure 16(a) indicate a frequency shift consistent with the frequency shift for the peak magnitude. (The predicted phase at the predicted frequency of peak response is in close agreement with the actual phase at the actual frequency of peak response.) Figure 16(b), which presents a polar plot of the curves of figure 16(a), illustrates the correspondence between the magnitude and phase frequency shifts. The phase correspondence between the measured and predicted curves is good, particularly in the vicinity of the peak response.

If a control law has dynamics in the flutter frequency range, the shifted plant dynamics can introduce potentially large phase shifts in the frequency response of the loop transfer function. Therefore, control law designers should be aware of the

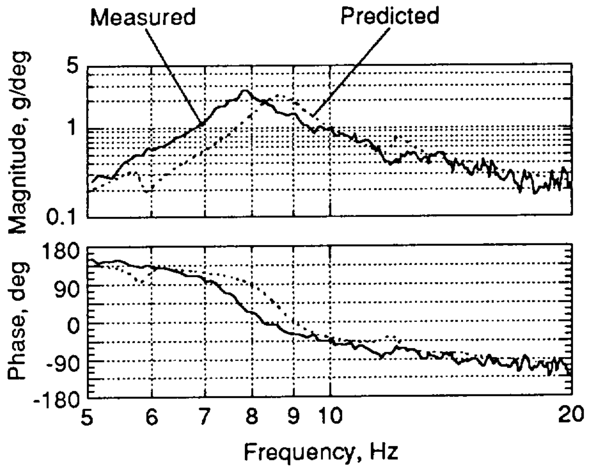

(a) Bode plot.

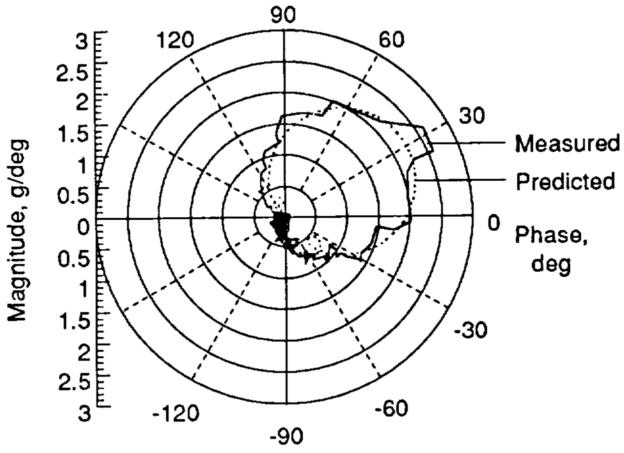

(b) Polar plot.

Figure 16. Predicted and measured open-loop frequency response for $\ddot{z}_{\mathrm{TIP}}$ resulting from $\delta_{\mathrm{TEO}_c}$; symmetric, 175-psf condition. (Predicted response includes effects of 25-Hz antialiasing filter and 0.5 time step delay.)

sensitivity of their designs to changes in the frequencies of critical modes and should not rely strictly on the adequacy of typical phase margin requirements.

Because none of the control laws was scheduled with dynamic pressure, it is more significant to compare the difference between measured and predicted frequencies at dynamic pressures that are the same percent away from the corresponding flutter dynamic pressures than it is to compare the difference between measured and predicted frequencies at a given dynamic pressure. The relevant frequency shift at flutter was approximately 2 Hz.

## Traditional Pole/Zero Loci Controller

The traditional pole/zero design demonstrated closed-loop stability up to a dynamic pressure of about 272 psf. This test represented an increase of approximately 24 percent relative to the observed open-loop flutter boundary. Flutter was suppressed simultaneously in both symmetries. The controller stabilized the model at the 272-psf condition as indicated by the decay of bursts of turbulence-induced system response. The wind tunnel was operated at this condition for several minutes while time histories for loads and for commanded control deflections resulting from tunnel turbulence were being recorded for rms analysis. The rms control rates were only about 25 deg/sec, which is one-third of the acceptable maximum. The wind-tunnel safety system was activated automatically after the model responded to a burst of larger amplitude turbulence and the structural loads exceeded preset limits. Because the control law stabilized the system and was also able to limit the amplitude of the flutter mode for lower turbulence levels with significant reserve rate capability, it is speculated that increasing the feedback gain would have kept the structural loads caused by turbulence to be within the prescribed limits, at least in the flutter frequency range; however, a reduced high-frequency gain margin and, possibly, smaller phase margins would have accompanied the feedback gain increase.

Figure 17 presents singular value assessments of the antisymmetric control law obtained using the controller performance evaluation (CPE) software (ref. 58) and experimental data. This control law provides two inputs to the plant and utilizes one sensor output. Figures 17(a) and 17(b) present singular values of the return difference matrices at the plant input and plant output, respectively. Large values (a value of 1 is large) for both sets of minimum singular values would indicate that the closed-loop system stability characteristics are tolerant to unstructured uncertainties at the plant input and output.

The relatively small minimum singular values at the plant input which are seen in figure 17(a) near 7 Hz would result from errors in the worst possible direction and are not necessarily likely or even physically realizable. Consequently, use of this figure to assess tolerance to errors may be quite conservative. Error sources that could occur include errors in individual control surface aerodynamic effectivenesses in the 7-Hz frequency region, in control surface mass coupling terms, and in gain and phase of commands from the controller to the individual actuators. The successful closed-loop tests demon-

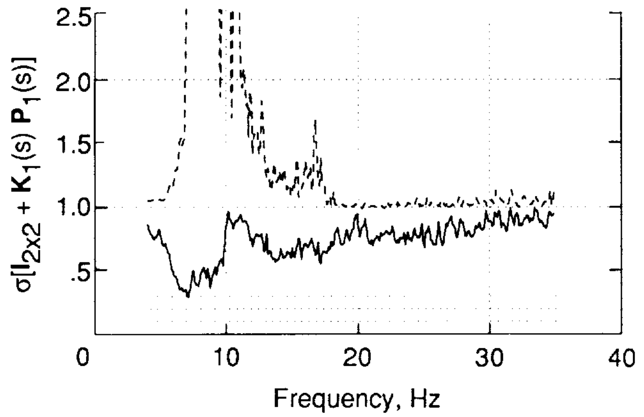

(a) Return difference at plant input; max is 9.69; min is 0.29 at 7.1 Hz.

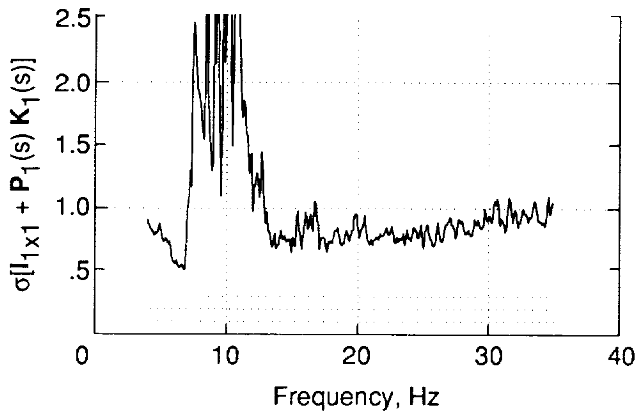

(b) Return difference at plant output; max is 4.71; min is 0.51 at 6.7 Hz.

Figure 17. Experimentally determined singular values for traditional pole/zero loci control; antisymmetric, 240-psf condition.

strated that the small but conservative assessment of tolerence to uncertainty of figure 17(a) was sufficient.

Only one singular value curve exists in figure 17(b) for the scalar plant output, and its magnitude corresponds to the distance of the single-strand Nyquist plot from the singular point. The singular values of figure 17(b) also correspond to the distance of the multi-input/single-output (MISO) Nyquist plot from the singular point. Figure 17(b) does not address distinct error sources in the two input channels, and, therefore, it is a potentially nonconservative assessment of robustness. Nevertheless, the test results demonstrated that the use of SISO robustness criteria to assess MISO robustness was adequate, in this case, to obtain a successful design. The global minimum near 7 Hz in figure 17 was associated with sensitivity to uncertainty in phase lead.

### Modal Rate Feedback Controller

The modal rate feedback controller that was designed based upon the predicted AFW wind-tunnel model characteristics was shown, by experimentally derived open-loop CPE, to be destabilizing at the two highest subcritical dynamic pressures tested (125 psf and 175 psf). The primary cause for these instabilities was believed to be undue sensitivity of the controller dynamics to frequency shifts of the critical structural modes.

Because the design method can readily employ experimentally derived frequency responses as inputs to the optimization, the frequencies of the controller dynamics were shifted to match the observed shift, and the blending matrix was reoptimized using transfer matrix estimates based upon data collected at 125 psf and 175 psf. No constraints were placed upon rms controller rate requirements because no experimentally derived frequency responses existed for outputs due to gust inputs. The numerical values of the parameters in the reoptimized control laws are shown in the appendix. Subsequent open-loop CPE and closed-loop testing with the redesigned controller showed that the system performance at 125 psf and 175 psf was in agreement with what had been predicted using the earlier experimental data. However, the controller destabilized the system at 185 psf with the instability occurring at a frequency of approximately 7 Hz. The source of the deficiency is discussed subsequently in the section entitled "Posttest Analysis."

### Modified LQG Controller

The modified LQG controller designed for 300 psf did not significantly change the closed-loop flutter dynamic pressure relative to the observed open-loop dynamic pressure. With this controller operating, antisymmetric flutter, at approximately 9.5 Hz, was encountered near the observed open-loop boundary of 220 psf. Data from the CPE analysis indicated a much lower antisymmetric component of control surface activity than predicted, which raised the possibility that the gain for the antisymmetric control law was too low. This aspect is discussed further in the section entitled "Posttest Analysis."

The controller designed for 350 psf was also tested. This 350-psf controller was very similar to the 300-psf controller, but it operated at higher gain levels. With the 350-psf controller operating, antisymmetric control surface activity was significantly higher, but the symmetric control law gain was too high in the 21-Hz region. The closed-loop system was driven symmetrically unstable at 175 psf at a frequency of approximately 21 Hz. Additional discussion of the sources of these difficulties is presented in the section entitled "Posttest Analysis."

### Combined Performance

Figure 18 shows the maximum closed-loop stable dynamic pressure achieved experimentally by each control law. Figure 19 depicts closed-loop control surface rms rates as functions of dynamic pressure. The rms rates were estimated by differentiating commanded deflections because rates were not commanded directly. The three plots represent the measured response for the three control laws during testing. Because the TEO control surfaces were dominant for each control law, rates are shown for the TEO surfaces.

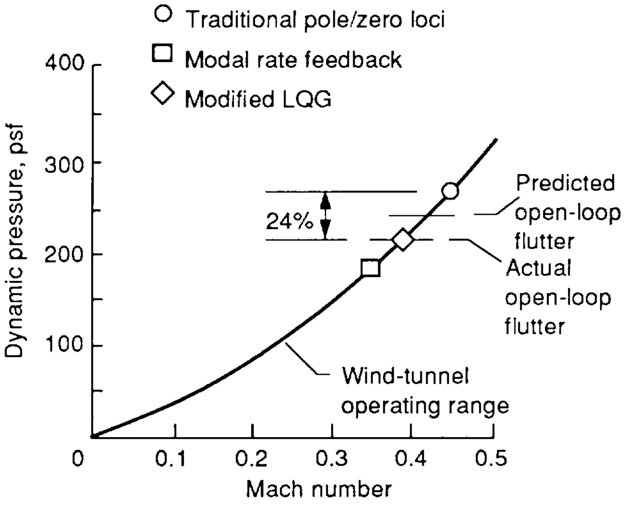

Figure 18. Maximum dynamic pressure obtained during closed-loop testing.

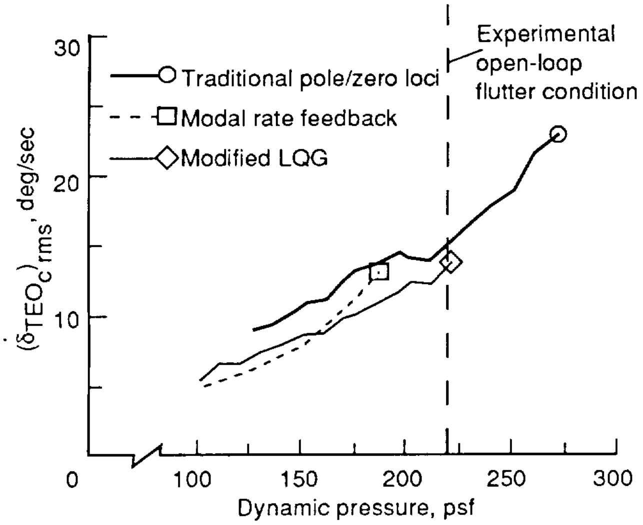

Figure 19. Experimentally determined root-mean-square (rms) control rates (design limit was 75 deg/sec rms).

All three control laws command similar levels of rms control surface activity at common dynamic pressures tested. This similarity reflects the fact that all three were designed with the same turbulence model and the same design limits. None of the control laws had difficulty staying within the design limit of 75°/sec rms. In fact, the peak measured rms rate is only approximately one-third of the limit for the traditional pole/zero design at 272 psf. The difference between predicted (see tables I, III, and IV) and measured rms control rate requirements may be because of errors in assumed turbulence levels and models, in control effectivenesses, and in modal damping. The low control surface rms rates indicate that additional control power is available for improved performance.

## Posttest Analysis

### Modal Rate Feedback Design

The test results clearly indicated that the pretest design and analysis associated with robustness assessments with respect to errors at the single-strand point (SISO) were insufficient. The basic problem was that, although there was an SISO point in the feedback loop, multiple sources existed for gain and phase errors, that is, four pairs of sensors and two pairs of controls. The optimization procedure did not consider control law performance sensitivities to multiple, independent errors. Singular value analysis of errors at the plant input and output points (fig. 9 shows the loop breaking points as dotted ovals) provides a means, although potentially quite conservative, to assess this sensitivity. Figure 20 graphically illustrates the deficiency of the design. This figure was generated using experimentally derived plant transfer matrix elements and the control law developed using the experimental data. This figure presents logarithmic plots of the minimum singular values of the return difference matrices at the single-strand point, the plant input point, and the plant output point for both symmetries. Large minimum singular values are desirable for robustness to error. Extremely small minimum singular values are evident for the return difference matrix at the plant output in a frequency range near 7 Hz.

The small minimum singular values were a result of the choice of objective function for controller parameter optimization. Consider the objective function (see eq. (7)) in the typical condition in which the

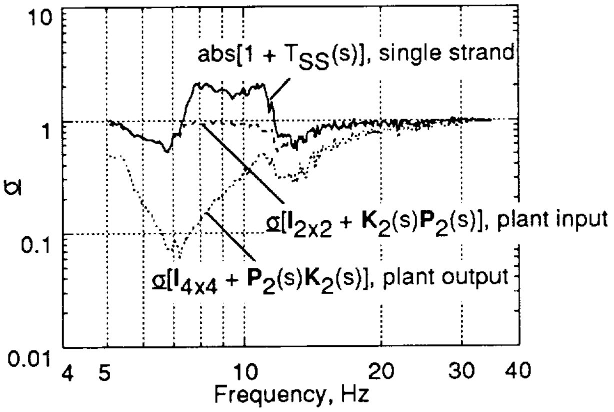

(a) Return differences at symmetric condition.

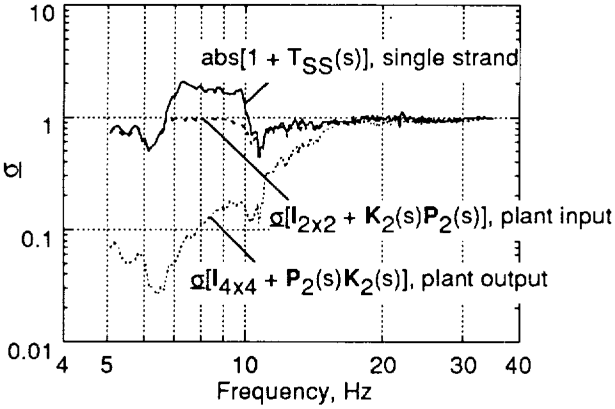

(b) Return differences at antisymmetric condition.

Figure 20. Experimentally determined minimum singular values for modal rate feedback control; 175-psf condition; law is derived from experimental data.

control rms constraints were inactive. In this condition, the optimization procedure was attempting to increase the nonconservative, upper bound SISO singular value abs$\{1 + T_{SS}(s)\}$ (ref. 35), and it was allowed to do so at the expense of the MIMO minimum singular values at the input $\underline{\sigma}[\mathbf{I} + \mathbf{K}_2(s)\mathbf{P}_2(s)]$ and the output $\underline{\sigma}[\mathbf{I} + \mathbf{P}_2(s)\mathbf{K}_2(s)]$. Extreme sensitivity of the closed-loop system to errors at the plant output resulted and led to destabilization by the controller. This result emphasizes the importance of properly capturing all the critical design trade-offs in either the objective function or in the design constraints.

### Modified LQG Design

The reduced-order controller developed using this design process and based upon a design point at 300 psf did not raise the closed-loop flutter dynamic pressure. The basic deficiency in the controller is shown in figures 21 and 22. Figure 21 shows two plots of the determinant of the matrix $[\mathbf{I} + \mathbf{P}_3(s)\mathbf{K}_3(s)]$, which is the MIMO Nyquist plot with zero as the critical point. The dashed curve shows predicted values, and the solid curve shows values derived from the experimental CPE analysis; both curves represent the antisymmetric condition at a dynamic pressure of 200 psf. The control law employed was the one based on the 300-psf design point. The smallness of the experimental curve relative to the analytical one is surprising. The test point of 200 psf is only 20 psf from the observed open-loop flutter dynamic pressure, whereas, for the analytical predictions, 200 psf is 52 psf from open-loop flutter. One would, therefore, expect the plant response to increase in amplitude much more in the test than in the analytical predictions. The indication is that the controller gain is too low. Figure 22 presents frequency responses for each channel of the continuous form of the reduced-order controller for each symmetry. (The washout filters are not included.) The antisymmetric control law has low gain in all channels in the 9-Hz to 10-Hz flutter frequency range as compared with the symmetric law. This difference in gain level is in contrast to the pole/zero loci law for which the dominant channel ($\delta_{\mathrm{TEO}_c}/\ddot{z}_{\mathrm{TIP}}$) was the same for both symmetries. The gain in the antisymmetric channels was not sufficient to suppress flutter; however, the size of the antisymmetric controller magnitude relative to the symmetric controller magnitude does not fully explain the drastic difference between the predicted and measured MIMO Nyquist curves in figure 21.

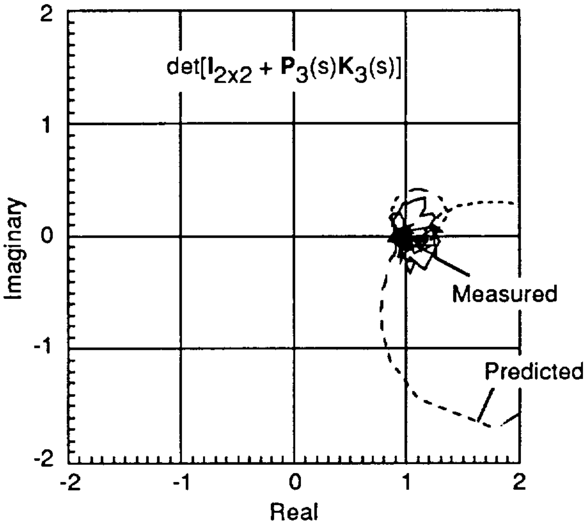

Figure 21. Predicted and measured multi-input/multi-output Nyquist plot for LQG law; antisymmetric, 200-psf condition; law is based on 300-psf design point.

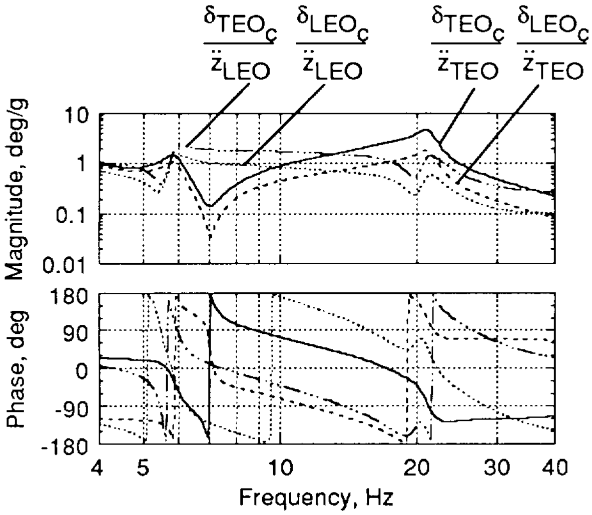

(a) Symmetric.

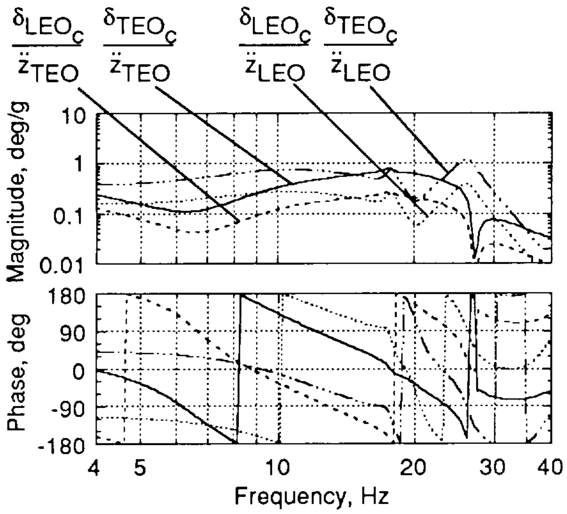

(b) Antisymmetric.

Figure 22. Frequency response for modified LQG controller designed at 300 psf.

The frequency responses for the controller design based upon the 350-psf point are shown in figure 23 and exhibit similar but higher gain characteristics as compared with the 300-psf design. Note the large amplitudes in the region of 21 Hz, particularly for $\delta_{TEO_c}/\ddot{z}_{TEO}$ for the symmetric law. This peak is present as a result of the recovery process and the existence of a lightly damped nonminimum phase transmission zero in the symmetric state-space model of the plant. The lowly damped controller pole is near the mirror image (with respect to the imaginary axis) of the nonminimum phase plant transmission zero. Such a factor makes the design susceptible to uncertainty in the plant characteristics near 21 Hz, which is a frequency approximately double the frequency to be controlled. This sensitivity is shown in figure 24, which presents predicted minimum singular values associated with the additive plant error at 200 psf for the symmetric degrees of freedom; the control law designed for the higher gain, 350-psf design point, was used. The figure reveals a controller stability robustness sensitivity to error not considered in the design process. An undesirably low minimum value occurs at a frequency near 21 Hz.

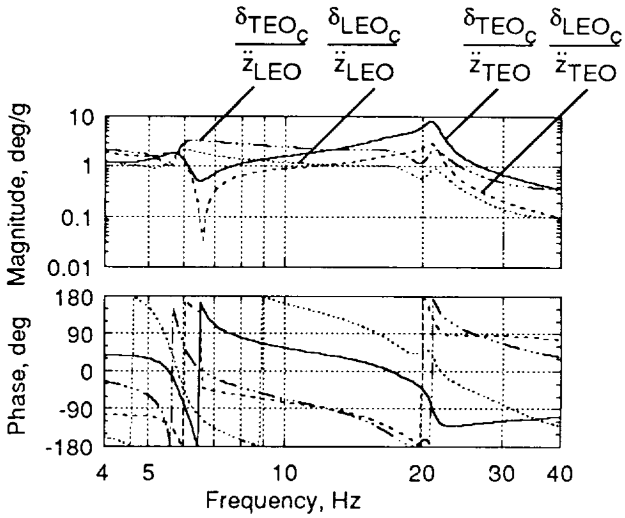

(a) Symmetric.

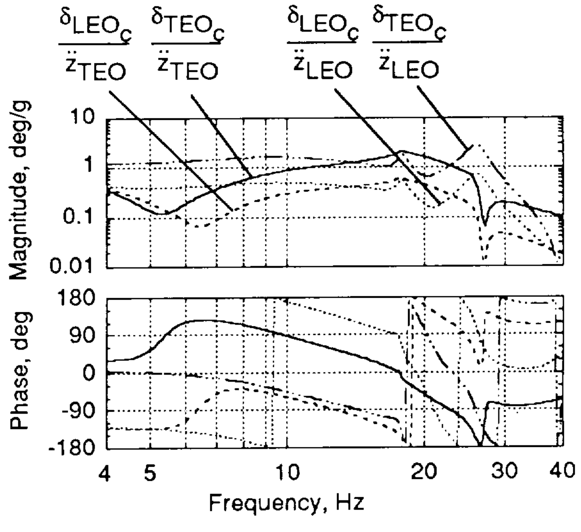

(b) Antisymmetric.

Figure 23. Frequency responses for modified LQG controller designed at 350 psf.

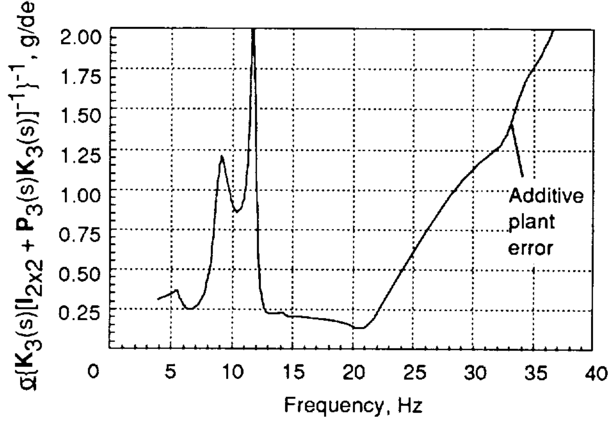

Figure 24. Predicted minimum singular value for modified LQG control; symmetric, 200-psf condition; law is based on 350-psf design point.

The high controller gain near 21 Hz, coupled with error between the predicted and actual plant, destabilized the closed-loop system during the test near 175 psf. It is conjectured that better performance would have been achieved with the antisymmetric law designed based upon the 350-psf point and the symmetric law designed based upon the 300-psf point.

## Concluding Remarks

Three flutter suppression control laws were designed in the continuous domain for the Rockwell International Corporation active flexible wing (AFW) wind-tunnel model. The control laws were implemented digitally and tested subsonically in the Langley Transonic Dynamics Tunnel at Langley Research Center. All three control laws were predicted to meet the objective of significantly raising the flutter onset dynamic pressure while not violating control surface rate and displacement limits.

Open-loop wind-tunnel testing exposed differences between predicted and actual AFW wind-tunnel model characteristics, particularly in the frequency of the flutter mode. However, the analytical model correctly captured the essential character of the flutter mechanism.

Only the traditional pole/zero loci design was sufficiently robust to the model errors to raise the closed-loop flutter dynamic pressure. With the pole/zero loci design, simultaneous suppression of symmetric and antisymmetric flutter was successfully demonstrated to a dynamic pressure 24 percent above the open-loop boundary. At this condition, the controller still provided stability as demonstrated by its succuessful damping of response resulting from typical bursts of turbulence over a period of 2 minutes; subsequently, however, a burst of larger amplitude turbulence caused torsional loads to exceed preset safety limits, at which point testing of this law was terminated.

The multi-input/multi-output modal rate feedback controller design process did not incorporate into the optimization procedure constraints upon critical sensitivities to errors at the plant output and to frequency shifts in the plant dynamics. This design led to inadequate robustness to the modeling errors that were encountered and closed-loop instability at a lower dynamic pressure than that of the observed open-loop condition.

The modified linear quadratic Gaussian controller design with subsequent controller order reduction was also sensitive to design model errors and did not have adequate guaranteed gain and phase margins. The sensitivity and robustness characteristics were strongly influenced by the presence of a lightly damped nonminimum phase transmission zero in the design model of the plant. As implemented, the design process placed a controller pole near the mirror image location, with respect to the imaginary axis, of the nonminimum phase zero. This placement not only resulted in undesirably high gain and sensitivity to plant error at a frequency that was double that of the mode to be controlled but also constrained the gain in the flutter frequency region. Closed-loop flutter was encountered during the test near the open-loop flutter dynamic pressure at the uncontrolled flutter frequency for a low-gain controller and below the open-loop flutter dynamic pressure at the frequency of the design model nonminimum phase transmission zero for a high-gain controller.

The November 1989 test provided data for assessing the fidelity of the analytical models of the AFW wind-tunnel model and for evaluating the robustness of the control laws to real-world implementation considerations. The lessons that were learned were applied in a subsequent effort in which four separate flutter suppression control laws were successfully tested not only in steady flight but also while performing aggressive, actively controlled, roll maneuvers.

NASA Langley Research Center
Hampton, VA 23681-0001
July 21, 1992

# Appendix

## Numerical Definition of Controller Parameters

The numerical values are specified here for the parameters in the continuous domain representation of the control laws that have been developed using each of the three design approaches. These definitions correspond to control laws tested in the Langley Transonic Dynamics Tunnel in November 1989. In each case, a digital implementation was carried out, prior to testing, using a Tustin transformation with no prewarping and a sample rate of 200 Hz.

### Traditional Pole/Zero Loci Control Law Definition

The parameters (see fig. 6 for their significance) have the same values for both symmetries. For the symmetric case, the switch is open in the channel commanding the trailing-edge inboard actuator pair.

$a = 5.000$ rad/sec (0.7958 Hz)

$\zeta_N = 0.4706$

$\omega_N = 85.00$ rad/sec (13.53 Hz)

$\zeta_D = 0.09950$

$\omega_D = 70.35$ rad/sec (11.20 Hz)

$k_1 = 0.4871$ deg/g (streamwise)

$d = -0.2500$

This design did not consider the effect of computational delay. Consequently, after applying the Tustin transformation, the "buy-back" procedure (see eqs. (2) and (3)) was employed to approximately counter the effect of the delay.

### Modal Rate Feedback Control Law Definition

Figure 9 shows the significance of the parameters.

$$\mathrm{AAF} = \frac{157}{s + 157} \qquad (25.0\ \mathrm{Hz})$$

$$\mathrm{BRF} = N_1 N_2 N_3$$

$$N_1 = \frac{s^2 + 2(0.08)(200)s + 200^2}{s^2 + 2(0.32)(200)s + 200^2} \qquad (31.8\ \mathrm{Hz})$$

$$N_2 = \frac{s^2 + 2(0.16)(250)s + 250^2}{s^2 + 2(0.48)(250)s + 250^2} \qquad (39.8\ \mathrm{Hz})$$

$$N_3 = \frac{s^2 + 2(0.12)(310)s + 310^2}{s^2 + 2(0.32)(310)s + 310^2} \qquad (49.3\ \mathrm{Hz})$$

$$\tau = 1.5T = 0.0075\ \mathrm{sec}$$

$$\mathrm{INT1} = \frac{1}{s + a_1}$$

$$\mathrm{INT2} = \frac{1}{s + a_2}$$

$$\mathrm{WOF} = \frac{s}{s + a}$$

$$\mathrm{DNOT} = \frac{s^2 + 2\zeta_N \omega_n s + \omega_n^2}{s^2 + 2\zeta_D \omega_n s + \omega_n^2}$$

$$\begin{bmatrix} \tilde{B}_1 \\ \tilde{B}_2 \end{bmatrix} = \mathbf{B}_{\mathrm{LN}} \begin{bmatrix} \ddot{z}_{\mathrm{LEO}} \\ \ddot{z}_{\mathrm{TEI}} \\ \ddot{z}_{\mathrm{TEO}} \\ \ddot{z}_{\mathrm{TIP}} \end{bmatrix}$$

$$\begin{bmatrix} \delta_{\mathrm{TEI}_c} \\ \delta_{\mathrm{TEO}_c} \end{bmatrix} = \mathbf{D}_{\mathrm{IS}} U$$

***Analytically derived control law.***

Symmetric:

$$\begin{array}{lcrll} a_1 & = & 4 & \text{rad/sec} & (0.6\ \text{Hz}) \\ a_2 & = & 30 & \text{rad/sec} & (4.8\ \text{Hz}) \\ a & = & 40 & \text{rad/sec} & (6.4\ \text{Hz}) \\ \omega_n & = & 36 & \text{rad/sec} & (5.7\ \text{Hz}) \\ \zeta_N & = & 0.03 & & \\ \zeta_D & = & 0.30 & & \end{array}$$

$$\mathbf{B}_{\mathrm{LN}} = \begin{bmatrix} [-0.3857 & 0.1187 & -0.0482 & 0.0780] & * \ 70 \\ [-0.5276 & 1.0000 & -0.5709 & 0.4476] & * \ 70^2 \end{bmatrix}$$

$$\mathbf{D}_{\mathrm{IS}} = \begin{bmatrix} 0.4500 \\ 1.0000 \end{bmatrix}$$

$$k_2 = -9.9251\ \text{deg/(g-sec)} \qquad \text{(degrees are streamwise)}$$

Antisymmetric:

$$\begin{array}{lcrll} a_1 & = & 6 & \text{rad/sec} & (1.0\ \text{Hz}) \\ a_2 & = & 56 & \text{rad/sec} & (8.9\ \text{Hz}) \\ a & = & 62 & \text{rad/sec} & (9.9\ \text{Hz}) \\ \omega_n & = & 115 & \text{rad/sec} & (18.3\ \text{Hz}) \\ \zeta_N & = & 0.03 & & \\ \zeta_D & = & 0.10 & & \end{array}$$

$$\mathbf{B}_{\mathrm{LN}} = \begin{bmatrix} [-0.5480 & 0.3341 & -0.1529 & 0.2053] & * \ 70 \\ [-0.4165 & 1.0000 & -0.7755 & 0.5353] & * \ 70^2 \end{bmatrix}$$

$$\mathbf{D}_{\mathrm{IS}} = \begin{bmatrix} 0.9000 \\ 1.0000 \end{bmatrix}$$

$$k_2 = -4.1000\ \text{deg/(g-sec)} \qquad \text{(degrees are streamwise)}$$

***Experimentally derived control law.***

Symmetric:

$a_1$ = 4 rad/sec (0.6 Hz)

$a_2$ = 17 rad/sec (2.7 Hz)

$a$ = 25 rad/sec (4.0 Hz)

$\omega_n$ = 33 rad/sec (5.3 Hz)

$\zeta_N$ = 0.06

$\zeta_D$ = 0.15

$$\mathbf{B}_{\mathrm{LN}} = \begin{bmatrix} [1.0000 & 0.0232 & -0.4618 & -0.1479] & * \ 70 \\ [0.3196 & 0.2871 & -0.0060 & -0.2931] & * \ 70^2 \end{bmatrix}$$

$$\mathbf{D}_{\mathrm{IS}} = \begin{bmatrix} 0.4500 \\ 1.0000 \end{bmatrix}$$

$k_2$ = 2.5000 deg/(g-sec) (degrees are streamwise)

Antisymmetric:

$a_1$ = 6 rad/sec (1.0 Hz)

$a_2$ = 38 rad/sec (6.0 Hz)

$a$ = 42 rad/sec (6.7 Hz)

$\omega_n$ = 103 rad/sec (16.4 Hz)

$\zeta_N$ = 0.03

$\zeta_D$ = 0.30

$$\mathbf{B}_{\mathrm{LN}} = \begin{bmatrix} [\ 0.1578 & -0.0867 & -0.1723 & 0.0677] & * \ 70 \\ [-0.3481 & 1.0000 & -0.1156 & -0.1151] & * \ 70^2 \end{bmatrix}$$

$$\mathbf{D}_{\mathrm{IS}} = \begin{bmatrix} 0.9000 \\ 1.0000 \end{bmatrix}$$

$k_2$ = 4.3000 deg/(g-sec) (degrees are streamwise)

### Modified LQG Control Laws

These matrices define the continuous controllers designed by the modified linear quadratic Gaussian (LQG) procedure followed by controller order reduction. Controller results are shown for design points at 300 psf and 350 psf. The design point upon which the controller is based is included as a subscript on the state matrices. Likewise, the subscript $S$ refers to symmetric and $A$ refers to antisymmetric. These matrices were designed with a Padé approximation of a 0.005-sec time delay included as part of the design plant (fig. 13). Figure 13 also shows elements added after the LQG design. These elements are analog notch filters ($N_1$ as defined in the section entitled "Modal Rate Feedback Control Law Definition" in this appendix) and washout filters ($a = 6$ rad/sec). The washout filters increase the digitally implemented order of the controller portion by 2 to 12. The inputs to the control laws are accelerations in gravitational units, and the outputs are commanded control deflections in degrees streamwise.

$$\mathbf{F}_{300_S} =$$

$$\begin{bmatrix} -10.2606 & 11.4264 & 0 & 0 & 0 & 0 & 0 & 0 & 0 & 0 \\ -11.4264 & -10.2606 & 0 & 0 & 0 & 0 & 0 & 0 & 0 & 0 \\ 0 & 0 & -1.8167 & 36.8465 & 0 & 0 & 0 & 0 & 0 & 0 \\ 0 & 0 & -36.8465 & -1.8167 & 0 & 0 & 0 & 0 & 0 & 0 \\ 0 & 0 & 0 & 0 & -29.4794 & 51.0219 & 0 & 0 & 0 & 0 \\ 0 & 0 & 0 & 0 & -51.0219 & -29.4794 & 0 & 0 & 0 & 0 \\ 0 & 0 & 0 & 0 & 0 & 0 & -25.7801 & 113.8901 & 0 & 0 \\ 0 & 0 & 0 & 0 & 0 & 0 & -113.8901 & -25.7801 & 0 & 0 \\ 0 & 0 & 0 & 0 & 0 & 0 & 0 & 0 & -6.0074 & 132.0979 \\ 0 & 0 & 0 & 0 & 0 & 0 & 0 & 0 & -132.0979 & -6.0074 \end{bmatrix}$$

$$\mathbf{G}_{300_S} =$$

$$\begin{bmatrix} 0.1044 & 0.1176 \\ -3.5706 & -5.6319 \\ -1.4527 & 0.7643 \\ 0.6457 & -0.2196 \\ 5.6922 & -4.3832 \\ -4.6252 & 2.4555 \\ 3.9561 & -3.8048 \\ -0.1957 & 0.4442 \\ 0.7371 & 0.5725 \\ -1.1023 & -3.1639 \end{bmatrix}$$

$$\mathbf{H}_{300_S} =$$

$$\begin{bmatrix} -6.9516 & -0.6589 & -3.0557 & 1.3527 & -5.9818 & 1.0610 & 8.6213 & -0.2974 & 4.2282 & 1.8143 \\ 8.7253 & -1.5487 & 3.0937 & -5.5602 & 10.7247 & -7.8683 & -22.1874 & 9.6035 & -14.2105 & -0.9051 \end{bmatrix}$$

$$\mathbf{E}_{300_S} =$$

$$\begin{bmatrix} -0.0710 & 0.0003 \\ 0.2204 & 0.0479 \end{bmatrix}$$

$\mathbf{F}_{300_A} =$

$$\begin{bmatrix}
-8.3952 & 8.9838 & 0 & 0 & 0 & 0 & 0 & 0 & 0 & 0 \\
-8.9838 & -8.3952 & 0 & 0 & 0 & 0 & 0 & 0 & 0 & 0 \\
0 & 0 & -28.5058 & 61.1189 & 0 & 0 & 0 & 0 & 0 & 0 \\
0 & 0 & -61.1189 & -28.5058 & 0 & 0 & 0 & 0 & 0 & 0 \\
0 & 0 & 0 & 0 & -2.8250 & 111.6667 & 0 & 0 & 0 & 0 \\
0 & 0 & 0 & 0 & -111.6667 & -2.8250 & 0 & 0 & 0 & 0 \\
0 & 0 & 0 & 0 & 0 & 0 & -28.0111 & 122.2674 & 0 & 0 \\
0 & 0 & 0 & 0 & 0 & 0 & -122.2674 & -28.0111 & 0 & 0 \\
0 & 0 & 0 & 0 & 0 & 0 & 0 & 0 & -8.2651 & 164.0179 \\
0 & 0 & 0 & 0 & 0 & 0 & 0 & 0 & -164.0179 & -8.2651
\end{bmatrix}$$

$\mathbf{G}_{300_A} =$

$$\begin{bmatrix}
-0.0364 & -0.0583 \\
1.9539 & 3.1044 \\
-2.1703 & 1.8668 \\
1.9796 & -1.0803 \\
-0.1316 & 0.2361 \\
0.8289 & 0.0775 \\
-2.4537 & 2.7932 \\
-1.5799 & 1.2050 \\
-0.0920 & -0.8088 \\
4.8785 & -0.6457
\end{bmatrix}$$

$\mathbf{H}_{300_A} =$

$$\begin{bmatrix}
2.5501 & 0.0272 & 5.3665 & -1.9025 & -0.9993 & 0.1522 & -4.2701 & 0.5809 & -1.2457 & 0.1270 \\
-5.9806 & 0.5921 & -15.6204 & 9.3613 & 3.4731 & -1.1375 & 14.5587 & -4.3242 & 4.4800 & -1.0030
\end{bmatrix}$$

$\mathbf{E}_{300A} =$

$$\begin{bmatrix}
-0.0018 & -0.0152 \\
0.0083 & 0.0617
\end{bmatrix}$$

$$\mathbf{F}_{350_S} =$$

$$\begin{bmatrix} -9.5757 & 10.8686 & 0 & 0 & 0 & 0 & 0 & 0 & 0 & 0 \\ -10.8686 & -9.5757 & 0 & 0 & 0 & 0 & 0 & 0 & 0 & 0 \\ 0 & 0 & -2.2954 & 36.7980 & 0 & 0 & 0 & 0 & 0 & 0 \\ 0 & 0 & -36.7980 & -2.2954 & 0 & 0 & 0 & 0 & 0 & 0 \\ 0 & 0 & 0 & 0 & -25.8883 & 41.6699 & 0 & 0 & 0 & 0 \\ 0 & 0 & 0 & 0 & -41.6699 & -25.8883 & 0 & 0 & 0 & 0 \\ 0 & 0 & 0 & 0 & 0 & 0 & -20.9726 & 111.5183 & 0 & 0 \\ 0 & 0 & 0 & 0 & 0 & 0 & -111.5183 & -20.9726 & 0 & 0 \\ 0 & 0 & 0 & 0 & 0 & 0 & 0 & 0 & -5.2954 & 132.0236 \\ 0 & 0 & 0 & 0 & 0 & 0 & 0 & 0 & -132.0236 & -5.2954 \end{bmatrix}$$

$$\mathbf{G}_{350_S} =$$

$$\begin{bmatrix} 0.5227 & -0.2915 \\ -4.1499 & -7.3690 \\ -4.7915 & 2.3804 \\ 0.0094 & 0.5254 \\ 7.7598 & -5.1526 \\ -3.8145 & 1.7785 \\ -3.3217 & 3.1583 \\ 2.3376 & -2.5772 \\ 2.0936 & 1.3330 \\ -0.9683 & -8.0868 \end{bmatrix}$$

$$\mathbf{H}_{350_S} =$$

$$\begin{bmatrix} -10.0640 & -1.4205 & -2.6514 & -0.1264 & -5.8140 & -0.3791 & -9.7835 & 1.4382 & 1.9375 & 1.6874 \\ 8.4008 & -2.2960 & 2.6435 & -3.5681 & 7.2858 & -9.7980 & 16.8243 & -19.1192 & -8.5543 & -0.9016 \end{bmatrix}$$

$$\mathbf{E}_{350_S} =$$

$$\begin{bmatrix} -0.0849 & 0.0238 \\ 0.2998 & 0.0567 \end{bmatrix}$$

$$\mathbf{F}_{350_A} =$$

$$\begin{bmatrix} -7.6193 & 8.5074 & 0 & 0 & 0 & 0 & 0 & 0 & 0 & 0 \\ -8.5074 & -7.6193 & 0 & 0 & 0 & 0 & 0 & 0 & 0 & 0 \\ 0 & 0 & -28.6342 & 53.7216 & 0 & 0 & 0 & 0 & 0 & 0 \\ 0 & 0 & -53.7216 & -28.6342 & 0 & 0 & 0 & 0 & 0 & 0 \\ 0 & 0 & 0 & 0 & -2.8832 & 111.9853 & 0 & 0 & 0 & 0 \\ 0 & 0 & 0 & 0 & -111.9853 & -2.8832 & 0 & 0 & 0 & 0 \\ 0 & 0 & 0 & 0 & 0 & 0 & -22.3533 & 120.0340 & 0 & 0 \\ 0 & 0 & 0 & 0 & 0 & 0 & -120.0340 & -22.3533 & 0 & 0 \\ 0 & 0 & 0 & 0 & 0 & 0 & 0 & 0 & -7.1933 & 163.7060 \\ 0 & 0 & 0 & 0 & 0 & 0 & 0 & 0 & -163.7060 & -7.1933 \end{bmatrix}$$

$$\mathbf{G}_{350_A} =$$

$$\begin{bmatrix} -0.2264 & -0.0472 \\ 3.0473 & 5.1245 \\ -5.8241 & 4.5198 \\ 3.7363 & -1.9123 \\ -0.1919 & 0.4602 \\ 1.2983 & -0.2419 \\ 2.9017 & -3.5133 \\ 1.9497 & -1.7576 \\ -0.1752 & -0.9363 \\ 6.8011 & -0.8170 \end{bmatrix}$$

$$\mathbf{H}_{350_A} =$$

$$\begin{bmatrix} 4.8726 & 0.5716 & 3.7646 & -0.2633 & -1.2795 & 0.1815 & 5.0504 & 0.9597 & -1.4415 & -0.1221 \\ -8.6031 & 0.8148 & -8.8879 & 7.9763 & 4.8913 & -3.1795 & -19.8503 & 6.3186 & 6.4734 & -1.6116 \end{bmatrix}$$

$$\mathbf{E}_{350_A} =$$

$$\begin{bmatrix} -0.0106 & -0.0132 \\ 0.0792 & 0.1139 \end{bmatrix}$$

## References

1. Wykes, John H.; and Mori, Alva S.: Techniques and Results of an Analytical Investigation Into Controlling the Structural Modes of Flexible Aircraft. *AIAA Symposium on Structural Dynamics and Aeroelasticity,* Aug.–Sept. 1965, pp. 419–433.
2. Burris, P. M.; and Bender, M. A.: *Aircraft Load Alleviation and Mode Stabilization (LAMS) Flight Demonstration Test Analysis.* AFFDL-TR-68-164, U.S. Air Force, Dec. 1969. (Available from DTIC as AD 865 310.)
3. Wykes, John H.; and Kordes, Eldon E.: Analytical Design and Flight Tests of a Modal Suppression System on the XB-70 Airplane. *Aeroelastic Effects From a Flight Mechanics Standpoint,* AGARD-CP-46, 1970, pp. 23-1–23-18.
4. Nissim, E.: *Flutter Suppression Using Active Controls Based Upon the Concept of Aerodynamic Energy.* NASA TN D-6199, 1971.
5. VanDierendonck, Albert J.; Stone, Charles R.; and Ward, Michael D.: *Application of Practical Optimal Control Theory to the C-5A Load Improvement Control System (LICS).* AFFDL-TR-73-122, U.S. Air Force, Oct. 1973. (Available from DTIC as AD 776 297.)
6. Triplett, William E.; Kappus, Hans-Peter F.; and Landy, Robert J.: Active Flutter Control: An Adaptable Application to Wing/Store Flutter. AIAA Paper No. 73-194, Jan. 1973.
7. Lyons, M. G.; Vepa, R.; McIntosh, S. C., Jr.; and DeBra, D. B.: Control Law Synthesis and Sensor Design for Active Flutter Suppression. AIAA Paper No. 73-832, Aug. 1973.
8. Peloubet, R. P., Jr.: YF16 Active-Control-System/Structural Dynamics Interaction Instability. AIAA Paper No. 75-823, May 1975.
9. Roger, Kenneth L.; Hodges, Garold E.; and Felt, Larry: Active Flutter Suppression—A Flight Test Demonstration. *J. Aircr.,* vol. 12, no. 6, June 1975, pp. 551–556.
10. Sandford, Maynard C.; Abel, Irving; and Gray, David L.: Transonic Study of Active Flutter Suppression Based on an Energy Concept. *J. Aircr.,* vol. 12, no. 2, Feb. 1975, pp. 72–77.
11. Harvey, C. A.; and Johnson, T. L.: *Adaptive Control of Wing/Store Flutter.* AFFDL-TR-79-3081, U.S. Air Force, Apr. 1979. (Available from DTIC as AD B042 335L.)
12. Newsom, Jerry R.: *A Method for Obtaining Practical Flutter-Suppression Control Laws Using Results of Optimal Control Theory.* NASA TP-1471, 1979.
13. Noll, T. E.; and Huttsell, L. J.: Wing Store Active Flutter Suppression—Correlation of Analyses and Wind-Tunnel Data. *J. Aircr.,* vol. 16, no. 7, July 1979, pp. 491–497.
14. Gangsaas, Dagfinn; and Ly, Uy-Loi: Application of a Modified Linear Quadratic Gaussian Design to Active Control of a Transport Airplane. AIAA Paper No. 79-1746, Aug. 1979.
15. Murrow, H. N.; and Eckstrom, C. V.: Drones for Aerodynamic and Structural Testing (DAST)—A Status Report. *J. Aircr.,* vol. 16, no. 8, Aug. 1979, pp. 521–526.
16. Mahesh, J. K.; Garrard, W. L.; Stone, C. R.; and Hausman, P. D.: *Active Flutter Control for Flexible Vehicles. Volume 1—Final Report.* NASA CR-159160, 1979.
17. Breitbach, Elmar J.: *Flutter Analysis of an Airplane With Multiple Structural Nonlinearities in the Control System.* NASA TP-1620, 1980.
18. Mukhopadhyay, V.; Newsom, J. R.; and Abel, I.: A Direct Method for Synthesizing Low-Order Optimal Feedback Control Laws With Application to Flutter Suppression. *A Collection of Technical Papers—Atmospheric Flight Mechanics Conference,* American Inst. of Aeronautics and Astronautics, Inc., Aug. 1980, pp. 465–475. (Available as AIAA-80-1613.)
19. Hwang, C.; Johnson, E. H.; Mills, G. R.; and Pi, W. S.: *Additional Demonstration of Active Wing/Store Flutter Suppression Systems.* AFWAL-TR-80-3093, U.S. Air Force, Aug. 1980. (Available from DTIC as AD B054 485.)
20. Adams, William M., Jr.; and Tiffany, Sherwood H.: *Control Law Design To Meet Constraints Using SYNPAC—Synthesis Package for Active Controls.* NASA TM-83264, 1982.
21. Ostroff, Aaron J.; and Pines, Samuel: *Application of Modal Control to Wing-Flutter Suppression.* NASA TP-1983, 1982.
22. Hanson, Perry W.: *An Aeroelastician's Perspective of Wind Tunnel and Flight Experiences With Active Control of Structural Response and Stability.* NASA TM-85761, 1984.
23. Adams, William M., Jr.; and Tiffany, Sherwood H.: *Design of a Candidate Flutter Suppression Control Law for DAST ARW-2.* NASA TM-86257, 1984.
24. Peloubet, R. P., Jr.; Haller, R. L.; and Bolding, R. M.: Recent Developments in the F-16 Flutter Suppression With Active Control Program. *J. Aircr.,* vol. 21, no. 9, Sept. 1984, pp. 716–721.
25. Van Gelder, P. A.: NLR Experience in the Application of Active Flutter Suppression and Gust Load Alleviation, Applied to a Wind-Tunnel Model. *Second International Symposium on Aeroelasticity and Structural Dynamics,* DGLR-Bericht 85-02, Deutsche Gesellschaft für Luft- und Raumfahrt e.V. (DGLR) (Bonn, W. Germany), 1985, pp. 320–329.
26. Kaynes, I. W.; Skingle, C. W.; and Copley, J. C.: The Design and Wind Tunnel Demonstration of an Active Control System for Gust Load Alleviation and Flutter Suppression. *Second International Symposium on Aeroelasticity and Structural Dynamics,* DGLR-Bericht 85-02, Deutsche Gesellschaft für Luft- und Raumfahrt e.V. (DGLR) (Bonn, W. Germany), 1985, pp. 330–347.
27. Schmidt, D. K.; and Chen, T. K.: Frequency Domain Synthesis of a Robust Flutter Suppression Control Law.

*J. Guid., Control, and Dyn.*, vol. 9, no. 3, May–June 1986, pp. 346–351.

28. Garrard, William L.; Liebst, Bradley S.; and Farm, Jerome A.: *Eigenspace Techniques for Active Flutter Suppression.* NASA CR-4071, 1987.

29. Freymann, R.: Interactions Between an Aircraft Structure and Active Control Systems. *J. Guid., Control, and Dyn.*, vol. 10, no. 5, Sept.–Oct. 1987, pp. 447–452.

30. Garrick, I. E.; and Reed, Wilmer H., III: Historical Development of Aircraft Flutter. *J. Aircr.*, vol. 18, no. 11, Nov. 1981, pp. 897–912. (Available as AIAA-81-0491R.)

31. Noll, Thomas E.; Perry, Boyd, III; Tiffany, Sherwood H.; Cole, Stanley R.; Buttrill, Carey S.; Adams, William M., Jr.; Houck, Jacob A.; Srinathkumar, S.; Mukhopadhyay, Vivek; Pototzky, Anthony S.; Heeg, Jennifer; McGraw, Sandra M.; Miller, Gerald; Ryan, Rosemary; Brosnan, Michael; Haverty, James; and Klepl, Martin: *Aeroservoelastic Wind-Tunnel Investigations Using the Active Flexible Wing Model—Status and Recent Accomplishments.* NASA TM-101570, 1989.

32. Perry, Boyd, III; Mukhopadhyay, Vivek; Hoadley, Sherwood Tiffany; Cole, Stanley R.; Buttrill, Carey S.; and Houck, Jacob A.: Design, Implementation, Simulation, and Testing of Digital Flutter Suppression Systems for the Active Flexible Wing Wind-Tunnel Model. *ICAS Proceedings 1990—17th Congress of the International Council of the Aeronautical Sciences,* 1990, pp. 408–418. (Available as ICAS-90-1.3.2.)

33. Miller, Gerald D.: *Active Flexible Wing (AFW) Technology.* AFWAL-TR-87-3096, U.S. Air Force, Feb. 1988.

34. Waszak, M. R.; and Srinathkumar, S.: Flutter Suppression for the Active Flexible Wing: Control System Design and Experimental Validation. *A Collection of Technical Papers—AIAA Dynamics Specialist Conference,* American Inst. of Aeronautics and Astronautics, Apr. 1992, pp. 138–145. (Available as AIAA-92-2097-CP.)

35. Christhilf, David M.; and Adams, William M., Jr.: Multifunction Tests of a Frequency Domain Based Flutter Suppression System. NASA TM-107615, 1992.

36. Mukhopadhyay, Vivek: Flutter Suppression Digital Control Law Design and Testing for the AFW Wind-Tunnel Model. *A Collection of Technical Papers—AIAA Dynamics Specialist Conference,* American Inst. of Aeronautics and Astronautics, Apr. 1992, pp. 156–161. (Available as AIAA-92-2095-CP.)

37. Klepl, M. J.: A Flutter Suppression System Using Strain Gages Applied to Active Flexible Wing Technology: Design and Test. *A Collection of Technical Papers—AIAA Dynamics Specialist Conference,* American Inst. of Aeronautics and Astronautics, Apr. 1992, pp. 162–171. (Available as AIAA-92-2098-CP.)

38. Ogata, Katsuhiko: *Modern Control Engineering.* Prentice-Hall, Inc., c.1970.

39. Doyle, John C.; and Stein, Gunter: Multivariable Feedback Design: Concepts for a Classical/Modern Synthesis. *IEEE Trans. Autom. Control,* vol. AC-26, no. 1, Feb. 1981, pp. 4–16.

40. Moore, Bruce C.: Principal Component Analysis in Linear Systems: Controllability, Observability, and Model Reduction. *IEEE Trans. Autom. Control,* vol. AC-26, no. 1, Feb. 1981, pp. 17–32.

41. Perry, Boyd, III; Dunn, H. J.; and Sandford, Maynard C.: Control Law Parameterization for an Aeroelastic Wind-Tunnel Model Equipped With an Active Roll Control System and Comparison With Experiment. *A Collection of Technical Papers, Part 1—AIAA/ASME/ASCE/AHS 29th Structures, Structural Dynamics and Materials Conference,* American Inst. of Aeronautics and Astronautics, Inc., Apr. 1988, pp. 41–56. (Available as AIAA-88-2211.)

42. Reed, Wilmer H., III; Cazier, F. W., Jr.; and Foughner, Jerome T., Jr.: *Passive Control of Wing/Store Flutter.* NASA TM-81865, 1980.

43. Perry, Boyd, III; Cole, Stanley R.; and Miller, Gerald D.: A Summary of the Active Flexible Wing Program. *A Collection of Technical Papers—AIAA Dynamics Specialist Conference,* American Inst. of Aeronautics and Astronautics, Apr. 1992, pp. 1–10. (Available as AIAA-92-2080-CP.)

44. Reed, Wilmer H., III: *Aeroelasticity Matters: Some Reflections on Two Decades of Testing in the NASA Langley Transonic Dynamics Tunnel.* NASA TM-83210, 1981.

45. Peele, Elwood L.; and Adams, William M., Jr.: *A Digital Program for Calculating the Interaction Between Flexible Structures, Unsteady Aerodynamics and Active Controls.* NASA TM-80040, 1979.

46. Giesing, Joseph P.; Kalman, Terez P.; and Rodden, William P.: *Subsonic Unsteady Aerodynamics for General Configurations. Part 1, Volume 1: Direct Application of the Nonplanar Doublet-Lattice Method.* AFFDL-TR-71-5-PT-1-VOL-1, U.S. Air Force, Nov. 1971. (Available from DTIC as AD 891 403L.)

47. Buttrill, Carey S.; and Houck, Jacob A.: Hot-Bench Simulation of the Active Flexible Wing Wind-Tunnel Model. *A Collection of Technical Papers—AIAA Flight Simulation Technologies Conference and Exhibit,* American Inst. of Aeronautics and Astronautics, Sept. 1990, pp. 11–21. (Available as AIAA-90-3121-CP.)

48. *Military Specification—Flying Qualities of Piloted Airplanes.* MIL-F-8785C, Nov. 5, 1980. (Supersedes MIL-F-8785B, Aug. 7, 1969.)

49. Tiffany, Sherwood H.; and Adams, William M., Jr.: *Nonlinear Programming Extensions to Rational Function Approximation Methods for Unsteady Aerodynamic Forces.* NASA TP-2776, 1988.

50. Hoadley, Sherwood T.; Buttrill, Carey S.; McGraw, Sandra M.; and Houck, Jacob A.: Development, Simulation Validation, and Wind-Tunnel Testing of a Digital Controller System for Flutter Suppression. *4th NASA Workshop on Computational Control of Flexible*

*Aerospace Systems,* Lawrence W. Taylor, Jr., compiler, NASA CP-10065, Part 2, 1991, pp. 583–613.

51. Franklin, Gene F.; and Powell, J. David: *Digital Control of Dynamic Systems.* Addison-Wesley Publ. Co., Inc., c.1980.

52. Newsom, Jerry R.; Abel, Irving; and Dunn, H. J.: *Application of Two Design Methods for Active Flutter Suppression and Wind-Tunnel Test Results.* NASA TP-1653, 1980.

53. Srinathkumar, S.; and Adams, W. M., Jr.: Active Flutter Suppression Using Invariant Zeros/Eigensystem Assignment. AIAA-89-3610, Aug. 1989.

54. Adams, William M., Jr.; Tiffany, Sherwood H.; and Bardusch, Richard E.: Active Suppression of an "Apparent Shock Induced Instability." *A Collection of Technical Papers, Part 2A AIAA/ASME 28th Structures, Structural Dynamics and Materials Conference,* American Inst. of Aeronautics and Astronautics, Apr. 1987, pp. 491–505. (Available as AIAA-87-0881.)

55. Fletcher, R.; and Powell, M. J. D.: A Rapidly Convergent Descent Method for Minimization. *Comput. J.,* vol. 6, no. 2, July 1963, pp. 163–168.

56. Kwakernaak, Huibert; and Sivan, Raphael: *Linear Optimal Control Systems.* John Wiley & Sons, Inc., c.1972.

57. Mukhopadhyay, V.; and Newsom, J. R.: A Multi-loop System Stability Margin Study Using Matrix Singular Values. *J. Guid., Control, and Dyn.,* vol. 7, no. 5, Sept.–Oct. 1984, pp. 582–587.

58. Pototzky, Anthony S.; Wieseman, Carol; Hoadley, Sherwood Tiffany; and Mukhopadhyay, Vivek: Development and Testing of Methodology for Evaluating the Performance of Multi-Input/Multi-Output Digital Control Systems. *A Collection of Technical Papers, Part 2 AIAA Guidance, Navigation and Control Conference,* American Inst. of Aeronautics and Astronautics, Aug. 1990, pp. 1673–1682. (Available as AIAA-90-3501-CP.)

| | |
|---|---|
| **REPORT DOCUMENTATION PAGE** | *Form Approved*<br>*OMB No. 0704-0188* |

Public reporting burden for this collection of information is estimated to average 1 hour per response, including the time for reviewing instructions, searching existing data sources, gathering and maintaining the data needed, and completing and reviewing the collection of information. Send comments regarding this burden estimate or any other aspect of this collection of information, including suggestions for reducing this burden, to Washington Headquarters Services, Directorate for Information Operations and Reports, 1215 Jefferson Davis Highway, Suite 1204, Arlington, VA 22202-4302, and to the Office of Management and Budget, Paperwork Reduction Project (0704-0188), Washington, DC 20503.

| | | |
|---|---|---|
| **1. AGENCY USE ONLY***(Leave blank)* | **2. REPORT DATE**<br>October 1992 | **3. REPORT TYPE AND DATES COVERED**<br>Technical Memorandum |

| | |
|---|---|
| **4. TITLE AND SUBTITLE**<br>Design, Test, and Evaluation of Three Active Flutter Suppression Controllers | **5. FUNDING NUMBERS**<br>WU 505-64-20-01 |
| **6. AUTHOR(S)**<br>William M. Adams, Jr., David M. Christhilf, Martin R. Waszak, Vivek Mukhopadhyay, and S. Srinathkumar | |
| **7. PERFORMING ORGANIZATION NAME(S) AND ADDRESS(ES)**<br>NASA Langley Research Center<br>Hampton, VA 23681-0001 | **8. PERFORMING ORGANIZATION REPORT NUMBER**<br>L-17041 |
| **9. SPONSORING/MONITORING AGENCY NAME(S) AND ADDRESS(ES)**<br>National Aeronautics and Space Administration<br>Washington, DC 20546-0001 | **10. SPONSORING/MONITORING AGENCY REPORT NUMBER**<br>NASA TM-4338 |

**11. SUPPLEMENTARY NOTES**

Adams, Waszak, and Mukhopadhyay: Langley Research Center, Hampton, VA; Christhilf: Lockheed Engineering & Sciences Co., Hampton, VA; Srinathkumar: National Aeronautical Laboratory, Bangalore, India.

| | |
|---|---|
| **12a. DISTRIBUTION/AVAILABILITY STATEMENT**<br>Unclassified–Unlimited<br>Subject Category 08 | **12b. DISTRIBUTION CODE** |

**13. ABSTRACT** *(Maximum 200 words)*

Three control law design techniques for flutter suppression are presented. Each technique uses multiple control surfaces and/or sensors. The first method uses traditional tools (such as pole/zero loci and Nyquist diagrams) for producing a controller that has minimal complexity and which is sufficiently robust to handle plant uncertainty. The second procedure uses linear combinations of several accelerometer signals and dynamic compensation to synthesize the modal rate of the critical mode for feedback to the distributed control surfaces. The third technique starts with a minimum-energy linear quadratic Gaussian controller, iteratively modifies intensity matrices corresponding to input and output noise, and applies controller order reduction to achieve a low-order, robust controller. The resulting designs have been implemented digitally and tested subsonically on the active flexible wing wind-tunnel model in the Langley Transonic Dynamics Tunnel. Only the traditional pole/zero loci design was sufficiently robust to errors in the nominal plant to successfully suppress flutter during the test. The traditional pole/zero loci design provided simultaneous suppression of symmetric and antisymmetric flutter with a 24-percent increase in attainable dynamic pressure. Posttest analyses are shown which illustrate the problems encountered with the other laws.

| | |
|---|---|
| **14. SUBJECT TERMS**<br>Flutter suppression; Wind-tunnel test; Active flexible wing; Classical, frequency domain multi-input/multi-output constrained optimization; Modified linear quadratic Gaussian/loop transfer recovery; Robustness | **15. NUMBER OF PAGES**<br>39 |
| | **16. PRICE CODE**<br>A03 |

| | | | |
|---|---|---|---|
| **17. SECURITY CLASSIFICATION OF REPORT**<br>Unclassified | **18. SECURITY CLASSIFICATION OF THIS PAGE**<br>Unclassified | **19. SECURITY CLASSIFICATION OF ABSTRACT** | **20. LIMITATION OF ABSTRACT** |

**NSN 7540-01-280-5500**

**Standard Form 298(Rev. 2-89)**
Prescribed by ANSI Std. Z39-18
298-102

NASA-Langley, 1992